Overview of Methods for Image Reconstruction From Projections in Emission Computed Tomography

ROBERT M. LEWITT, SENIOR MEMBER, IEEE, AND SAMUEL MATEJ, SENIOR MEMBER, IEEE

Invited Paper

Emission computed tomography (ECT) is a technology for medical imaging whose importance is increasing rapidly. There is a growing appreciation for the value of the functional (as opposed to anatomical) information that is provided by ECT and there are significant advancements taking place, both in the instrumentation for data collection, and in the computer methods for generating images from the measured data. These computer methods are designed to solve the inverse problem known as "image reconstruction from projections." This paper uses the various models of the data collection process as the framework for presenting an overview of the wide variety of methods that have been developed for image reconstruction in the major subfields of ECT, which are positron emission tomography (PET) and single-photon emission computed tomography (SPECT). The overall sequence of the major sections in the paper, and the presentation within each major section, both proceed from the more realistic and general models to those that are idealized and application specific. For most of the topics, the description proceeds from the three-dimensional case to the two-dimensional case. The paper presents a broad overview of algorithms for PET and SPECT, giving references to the literature where these algorithms and their applications are described in more detail.

Keywords*—*Emission tomography, image reconstruction from projections, inverse problems, positron emission tomography (PET), single-photon emission computed tomography (SPECT).

I. INTRODUCTION

Emission computed tomography (ECT) is a technology for medical imaging whose importance is increasing rapidly. There is a growing appreciation of the significance of the functional (as opposed to anatomical) information that is provided by ECT, and of its value for the purposes of medical diagnosis and monitoring the response to therapy. There are also significant advancements taking place, both in the instrumentation for data collection and in the computer methods for generating images from the measured data. These computer methods are designed to solve the inverse problem known as "image reconstruction from projections."

The major subfields of ECT are positron emission tomography (PET) and single-photon emission computed tomography (SPECT). The purpose of this paper is to give an overview of the computer algorithms that are used in PET and SPECT to generate images from the measured data. The design and implementation of these algorithms is a multidisciplinary effort involving techniques from electrical engineering (specifically, signal processing), computer science (data structures, software engineering), physics (modeling of radiation transport and detection processes), mathematics (functional analysis, optimization, numerical analysis), and statistics (random processes, statistical estimation theory). This paper is aimed toward readers having a background in electrical engineering, or one of the other disciplines mentioned above, but who are not familiar with algorithms for the inverse problem of ECT.

The paper presents a broad overview of algorithms for PET and SPECT, without going into the details of any specific topic in this field, since detailed descriptions of the specific topics within the scope of this paper may be found in the referenced survey papers, selected topical papers, special issues of journals, and books. This literature, in turn, contains references to a very large number of specialized papers relevant to some aspect of algorithms for reconstruction of images from projection data.

II. BRIEF OUTLINE OF DATA COLLECTION IN EMISSION TOMOGRAPHY

The goal of the radiology specialty of nuclear medicine, which includes PET and SPECT, is to provide information

Manuscript received July 15, 2002; revised March 17, 2003. This work was supported by the National Institutes of Health under Grant CA92060/EB002131 and Grant CA93962/EB002135.

The authors are with the Medical Image Processing Group, Department of Radiology, University of Pennsylvania, Philadelphia, PA 19104-6021, USA (e-mail: robert@mipg.upenn.edu; matej@mipg.upenn.edu).

Digital Object Identifier 10.1109/JPROC.2003.817882

on the distribution of a chosen molecule in space (and possibly also in time) inside the human body. For a molecule of biochemical or physiological importance, an image of its distribution within the body or a specific organ provides information on the functioning of the body or organ (including information on the locations of abnormalities such as cancer tumors) that is valuable for medical diagnosis and for monitoring the response to the treatment of disease.

The functional information obtained by PET and SPECT is complementary to the anatomical information that is available from other radiological imaging techniques, such as X-ray-computed tomography (CT) and magnetic resonance imaging (MRI). SPECT is firmly established as an important tool for evaluating the functional status of the heart muscle and its blood supply in order to determine if surgery would lead to any improvement in cardiac function. Although the majority of SPECT scans at the present time are done for the diagnosis of cardiac disease, there are many other clinical and research applications where SPECT is used. PET is rapidly emerging as an important tool for detecting cancer tumors and for evaluating their degree of malignancy, based on differences in biochemistry and metabolism between tumors and their surrounding normal tissues. Although cancer applications are the driving force behind the explosive increase in PET imaging at the present time, PET (like SPECT) continues to be used in a wide variety of clinical and research applications where functional information is required. Fig. 1 shows an example of an image obtained using PET.

The techniques used in nuclear medicine involve labeling the chosen molecule with a radioactive atom and administering a dose of the labeled molecules to the patient. The labeled molecules follow their specific biochemical pathways inside the body. The atoms used as labels are unstable isotopes and undergo radioactive decay at random, leading to the emission of gamma ray photons which can be detected outside the body by the detector system of a PET or SPECT scanner. Fig. 2 shows a typical PET scanner and the corresponding coordinate system used in the paper.

The label atoms used for SPECT each emit a single photon when they decay. The direction of the photon path is random for each emitted photon. The label atoms used for PET decay by emitting a positron, which is the antiparticle of the electron, having the same mass but with a positive charge. Within a short distance (usually less than 1 mm), the positron combines with an electron in an "annihilation event" (matter combining with anti-matter, mass converted to energy) which produces two back-to-back gamma ray photons, each of energy 511 keV and traveling in opposite directions along the same line (of random orientation).

The instrumentation for detecting gamma rays emerging from the body is different for PET and SPECT. We first describe the detection of gamma rays in PET, as illustrated in Fig. 3.

The useful data in PET result from the situation where the two photons emerge from the body without any interaction with the material of the body, and each photon is intercepted by the detector system. When two photons are detected at almost the same time, the coordinates of each photon interception are recorded by the detector system, and the assumption is made that these photons originated from an annihilation at some point along the line in space between the two points at which the photons were detected.

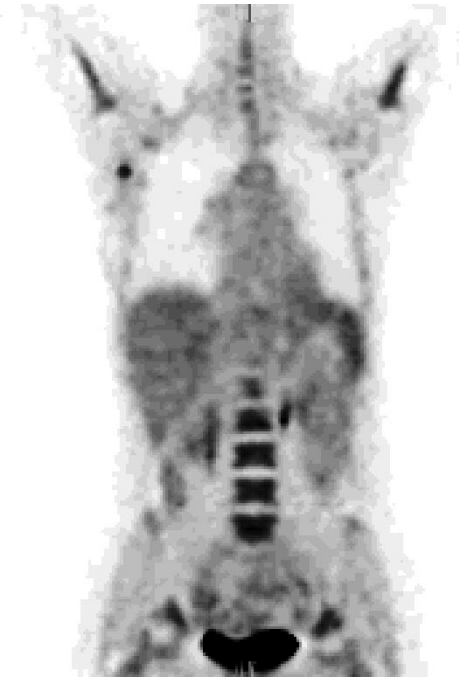

Fig. 1. Clinical whole-body PET study of a melanoma patient using FDG (i.e., deoxy-glucose labeled with Fluorine-18). The FDG is highly accumulated in the lesions as illustrated by the coronal slice containing a lesion in the axilla (i.e., armpit region). The image was reconstructed by a fully three–dimensional (3-D) iterative reconstruction algorithm (3-D RAMLA using blob basis functions) from approximately 15 million histogram bins of data (23 million coincidence counts) per bed position, with eight bed positions having 50% overlap. (The study was done at the PET Center in the Department of Radiology, University of Pennsylvania Medical Center).

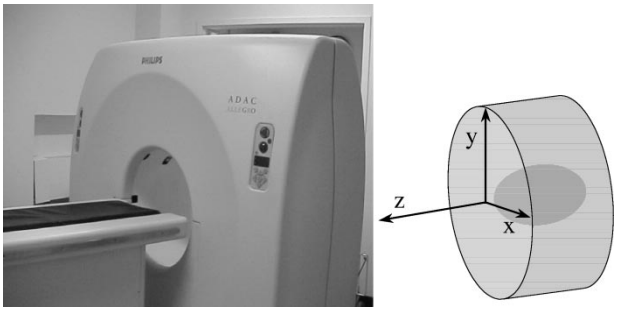

Fig. 2. A typical PET scanner, with a diagram of the coordinate system used in the paper showing its relationship to the physical scanner and patient bed.

This situation is called a "true coincidence," when two photons from the same positron-electron annihilation travel without interaction to the detector and both are detected within a short time window (typically, 6–12 ns). If one of the photons misses the detector for some reason, the time window will usually contain only one detected photon and the coordinates will be discarded, unless the same situation arises with another annihilation at almost the same time.

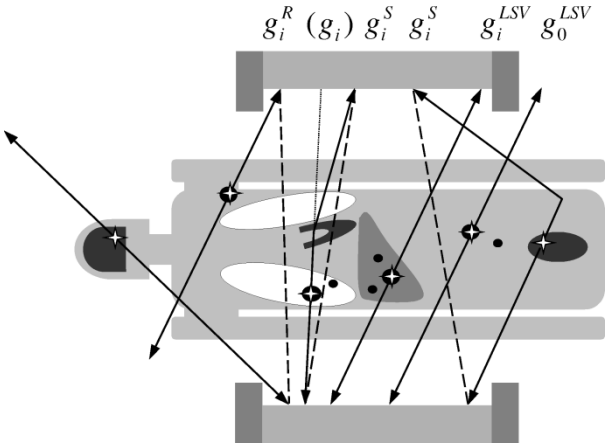

Fig. 3. Illustration of different photon paths in a PET scanner. The scanner may consist of a continuous detector forming a ring around the patient, or a pair of opposing detectors that rotates around the patient (coronal view shown). Black color indicates radioactive tracer in organ regions and tumors. Star symbol indicates the location of an annihilation event where a photon pair originates. Black line with an arrow represents the spatial path of an individual photon. Some photon paths and other lines have labels corresponding to the notation introduced in Section III. g_i^{LSV} represents ith line of response (LOR) showing a true coincidence, i.e., both photons originate from a point on this straight line. g_0^{LSV} illustrates an oblique line for a photon pair originating from within the scanner, for which only a single photon is detected (the other photon misses the detector surface). Dashed lines represent nontrue LOR's for individual photon pairs (detected within a time coincidence window) as interpreted by the detector system. g_i^{R} represents a dashed LOR for which a random coincidence was detected. The two g_i^{S} examples show dashed LORs for scatter coincidences, for which one of the photons was scattered after originating inside or outside the scanner field of view. (g_i) represents the original line from which one photon was lost (resulting in attenuation loss for this line) due to scatter of the photon.

This case is called a "random coincidence" (or "accidental coincidence") and is a source of error in the data, since the two detected photons come from different annihilations, neither of which is on the line in space joining the coordinates of the detected photons.

Two other sources of error occur when one photon (or both) interacts with the material and is deflected in a new direction. This results in a loss of counts ("attenuation") for the true straight line path, and is therefore a source of error in the data. If one photon (or both) is deflected from its original path and then both are detected, the result is a "scatter coincidence." This is also a source of error in the data, since the original annihilation is not on the line in space joining the coordinates of the detected photons, as illustrated in Fig. 3.

We now briefly describe the detection of gamma rays in SPECT, as illustrated in Fig. 4. In SPECT, each radioactive decay produces one photon (having energy 140 keV for the most commonly used radioactive label, Technetium-99m) that travels from the point of decay to the detector. Each element of the detector receives photons from a narrow cone of directions, defined by the physical aperture of a collimator device that rejects most of the incoming photons. The most common form of collimator consists of a thick slab of shielding material (e.g., lead, typical thickness 30–40 mm) having a large number of small diameter holes through

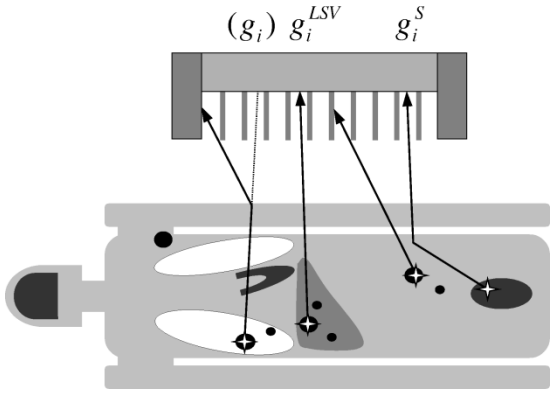

Fig. 4. Illustration of different photon paths in a SPECT scanner. The scanner may consist of one collimated detector (as shown) that rotates around the patient, or multiple collimated detectors arranged around the patient (coronal view shown). Black color indicates radioactive tracer in organ regions and tumors. Star symbol indicates the location where a single photon originates. Black line with an arrow represents the spatial path of an individual photon. Some photon paths (and another line) have labels corresponding to the notation introduced in Section III. g_i^{LSV} represents a true count recorded by the detector from a photon that was accepted by the parallel hole collimator and was not scattered from its original straight-line path. The photons traveling on oblique lines with respect to the collimator are rejected by the collimator (in practice, some penetration occurs). g_i^{S} represents detection of a scattered photon, which could originate from inside or outside the scanner field of view. (g_i) represents the original line from which the photon was lost (resulting in attenuation loss for this line) due to scatter of the photon.

it (typical diameter 1.5–2.5 mm) and placed adjacent to the front surface of the detector. Another form of collimator consists of a single pinhole aperture (typical diameter 0.5–2 mm) in a sheet of shielding material that is placed some distance (e.g., 150 mm) from the front surface of the detector, similar to the pinhole camera for visible-light photons. In SPECT, the detector accumulates those photons that pass through the collimator and that did not interact with the attenuating material on their path through the body. In practice, some scattered photons are also detected, as illustrated in Fig. 4.

In both PET and SPECT, the detector system accumulates counts for lines in space (actually, tube-shaped volumes), where the counts are individual photons in SPECT and are pairs of photons in time coincidence in PET. These counts include the effects of attenuation, scatter, and (in the case of PET) random coincidences. Apart from these effects, the total accumulated count for each line indicates the total number of label atoms along the line that underwent radioactive decay, but it does not indicate where these atoms were located along the line. The purpose of the image reconstruction algorithm is to process this imperfect count data for a large number (often millions) of lines and millions of detected photons to produce an image showing the distribution in space of the label atoms, and hence the distribution of the labeled molecules.

A. Notes and References

A fascinating book [1] describes the long history of tomographic imaging in radiology (i.e., imaging of cross sections

of the body) using X-ray photons and gamma-ray photons. The following books describe nuclear medicine physics and instrumentation [2], fundamentals of radiological imaging using X-rays and gamma rays [3], and the broad scope of medical imaging techniques [4]–[8]. The following books are specifically devoted to CT [9], MRI [10], [11], SPECT [12] and PET [13]. Detailed review articles that describe the physics and instrumentation associated with emission imaging include [14]–[17].

The topics described in the present paper, and many more, are treated in detail in the comprehensive book of Barrett and Myers [18], which includes a detailed exposition of approaches to evaluate the suitability of images for their intended purposes.

III. Problem Formulation for Emission Tomography

Many applications where indirect imaging is employed, including ECT, involve discrete measurements that correspond to some integral transformation of a function of continuous spatial variables, where the function and the image to be reconstructed from the data both represent the spatial distribution of some physical property of interest inside the object being imaged. In these applications, the process of data collection is naturally represented by a discrete-continuous (D-C) model that relates the discrete data to the function of continuous spatial variables, denoted here by $f(x,y,z)$.

In this paper, we assume that there is a linear, spatially variant (LSV) relationship between the basic physical component of the data and the function $f(x,y,z)$ that represents the spatial distribution. We first describe the LSV model, and we then build upon this basic physical model to obtain a more complete model of the data.

The LSV model is a good description of the basic physics of data collection in ECT, where the detector response is close to linear over the range of count rates found in most imaging applications, but the detector response may have significant variation with position. To specify the LSV model, we denote the corresponding component of the ith measurement by $\bar{g}_i^{\mathrm{LSV}}$, and we denote by $h_i(x,y,z)$ the contribution to the ith measurement of a point of unit strength located at (x,y,z). The basic physical model (D-C, LSV) of the data collection process, with the number of measurements denoted by I, is

$$\bar{g}_i^{\mathrm{LSV}} = \iiint_{\Omega} f(x,y,z)\, h_i(x,y,z)\, dx\, dy\, dz, \quad i = 1, \ldots, I \tag{1}$$

where Ω denotes the finite domain of the spatial distribution.

In emission tomography, the integration kernel $h_i(x,y,z)$ has nonzero value inside a tube-shaped region of space, and has zero value outside this tube, so that the ith measurement is modeled as the integral of $f(x,y,z)$, with a weighting of $h_i(x,y,z)$, over the ith tube. The tube-like shape of the integration kernel is the distinguishing characteristic of the problem of image reconstruction from projections, compared to the problem of image restoration from a blurred image, where the integration kernel is usually much more localized.

For both PET and SPECT, we choose to include in the integration kernel $h_i(x,y,z)$ the effect of photon attenuation on the measurements, although in the case of PET a factor representing attenuation can be separated from the kernel, as described in Sections VI-C, VII-A, and VII-B. In the following formulation, we choose to represent the contribution of the scattered photons to the data as an additive term separate from $\bar{g}_i^{\mathrm{LSV}}$, although the scatter contribution is a linear function of $f(x,y,z)$, and could therefore be included in the kernel, which would then have a much broader region of support (compared to the tube-shaped region when the kernel does not include scatter). In the case of PET, note that the contribution of the random coincidences to the data is a nonlinear function of $f(x,y,z)$ (proportional to f^2, see, e.g., [2]), and therefore cannot be included in the integration kernel $h_i(x,y,z)$. We represent the contribution of the random coincidences to the PET data as an additive term that will be estimated separately, similar to the term representing the scatter contribution.

We now describe a more complete model of the measurement process in emission tomography. For the PET case, we denote the ith measurement in the data set by g_i^{PET}, with similar notation g_i^{SPECT} for the SPECT case. Since each measurement is obtained by counting photons produced by a random emission process, g_i^{PET} and g_i^{SPECT} are samples (realizations) of random variables whose means (expected values) are denoted by $\mathrm{E}[g_i^{\mathrm{PET}}]$ and $\mathrm{E}[g_i^{\mathrm{SPECT}}]$.

In the measurement process for PET, which involves detection of pairs of emitted photons in time coincidence, the mean for the ith tube consists of the basic physical component $\bar{g}_i^{\mathrm{LSV}}$, and two additional (unwanted) components representing the additive contributions of the mean of the random coincidences, denoted by $\bar{g}_i^{\mathrm{R}}$, and the mean of the scatter coincidences, denoted by $\bar{g}_i^{\mathrm{S}}$. Thus, we have

$$\mathrm{E}[g_i^{\mathrm{PET}}] = \bar{g}_i^{\mathrm{LSV}} + \bar{g}_i^{\mathrm{R}} + \bar{g}_i^{\mathrm{S}}\,. \tag{2}$$

It can be shown that the probability distribution for each of the three components is Poisson about its respective mean, and we recall that the Poisson distribution $Poisson\{\lambda\}$ with mean λ has the property that the variance is equal to the mean. Therefore,

$$g_i^{\mathrm{PET}} = Poisson\{\bar{g}_i^{\mathrm{LSV}}\} + Poisson\{\bar{g}_i^{\mathrm{R}}\} + Poisson\{\bar{g}_i^{\mathrm{S}}\} \tag{3}$$

$$= Poisson\{\bar{g}_i^{\mathrm{LSV}} + \bar{g}_i^{\mathrm{R}} + \bar{g}_i^{\mathrm{S}}\}\,. \tag{4}$$

For the SPECT case, which involves detection of single emitted photons, the general structure of the model is similar except that the random coincidences component is not present. Therefore,

$$g_i^{\mathrm{SPECT}} = Poisson\{\bar{g}_i^{\mathrm{LSV}}\} + Poisson\{\bar{g}_i^{\mathrm{S}}\} \tag{5}$$

$$= Poisson\{\bar{g}_i^{\mathrm{LSV}} + \bar{g}_i^{\mathrm{S}}\}\,. \tag{6}$$

The kernel function $h_i(x,y,z)$, the LSV term $\bar{g}_i^{\mathrm{LSV}}$, and the scatter contribution $\bar{g}_i^{\mathrm{S}}$ are of course different in the SPECT

case from those in PET, but we avoid indicating this explicitly in the notation when the meaning is clear from the context.

From this point, we can take the D-C model and proceed in three different directions.

- Obtain a discrete-discrete (D-D) model from the D-C model by representing the unknown function $f(x,y,z)$ by a linear combination of a finite number of basis functions. Each of the basis functions is multiplied by a coefficient which is initially unknown, and is determined from the data by a specified computer algorithm. We discuss this approach in Section V.
- Obtain a continuous-continuous (C-C) model from the D-C model by interpreting the discrete data $\{g_i^{\mathrm{PET}}\}_{i=1}^I$ or $\{g_i^{\mathrm{SPECT}}\}_{i=1}^I$ as samples of a function of continuous variables in the measurement space. For the simplest forms of integration kernel $h_i(x,y,z)$ and measurement geometry, it is possible to derive an inversion formula expressing $f(x,y,z)$ in terms of the function of the measurement space variables. Numerical evaluation of the inversion formula produces samples $f(x_k,y_k,z_k)$ on a grid of points in image space, using the discrete data $\{g_i^{\mathrm{PET}}\}_{i=1}^I$ or $\{g_i^{\mathrm{SPECT}}\}_{i=1}^I$. We discuss this approach in Section VI.
- Proceed further with the D-C model. This leads to an approach in which the set of functions $\{h_i(x,y,z)\}_{i=1}^I$ becomes the set of basis functions in the image space. We discuss this approach in Section IV.

A. Notes and References

The various linear models (D-C, D-D, C-C) of data collection in the context of imaging are described in [18]–[21]. Modeling of the data collection process is described for PET [22], [23], for SPECT [24], [25], and for both [26]. The emission and detection of the photons in PET and SPECT involves random processes in time and space [27], and the derivation from first principles of the commonly used Poisson distribution requires a number of steps and assumptions [26]. The review paper [28] discusses the general topic of inverse problems from the statistical point of view.

The response of practical detectors degrades as the count rate increases because of "dead time" associated with the detection process for each incoming photon. Dead time introduces nonlinearity into the data collection process and affects the statistical distribution of the data. Although corrections for dead time may be introduced to restore the linearity of response up to some limiting count rate, the corrections also affect the statistical distribution of the data. A detailed discussion is given in [29] and [30]. In the present paper we describe reconstruction approaches that are based on linear models, which do not include the effects of dead time.

In SPECT, the most commonly used collimators have parallel holes to select incoming photons from a defined range of directions, but a wide variety of other collimation devices have been developed. These include rotating slant-hole collimators [31], [32], rotating slat collimators [33], pinhole collimators [34]–[36], and various converging beam collimators having fan-beam geometry [37], cone-beam geometry [38]–[40], and variable-focal-length geometry [41], [42]. Each of these data collection schemes has its own extensive literature—the few references cited here are intended to give examples of recent work on these topics and to provide entry points to the literature.

We note that there have been some efforts over the years (but with only limited success to date) to develop so-called time-of-flight (TOF) PET scanners capable of measuring (approximately) the difference between the times of detection of the two photons in the coincidence acceptance window; see, e.g., [43]. The physical processes of photon detection and the processes of position determination by the detector system result in an uncertainty in the time difference that is typically 0.5 ns, which corresponds to a localization uncertainty of 7.5 cm along the tube between the opposing detector elements. For TOF-PET, the measurement process may again be modeled by (1), but in this case the integration kernel $h_i(x,y,z)$ has a region of support that is only a segment of the tube-shaped region of support that it has for conventional PET. For TOF-PET, the reconstruction approaches based on the D-C and D-D models have the same structure as those for conventional PET. However, the inversion formulas derived from the C-C model for the conventional case are not applicable to TOF-PET.

IV. Image Reconstruction Approach Based on D-C Model

This approach leads to a direct solution to the fundamental D-C problem without introducing further discretization or approximation. Although the approach has this attractive theoretical property, the methods based on it are not widely used in PET or SPECT, so our description of this approach is more brief than that of the other approaches.

We interpret each of the $\bar{g}_i^{\mathrm{LSV}}$ in (1) as the inner product of the function $f(x,y,z)$ and the function $h_i(x,y,z)$. We denote by P the linear operator that operates on $f(x,y,z)$, as defined by (1), to produce the data-space vector $\bar{g}^{\mathrm{LSV}} = (\bar{g}_1^{\mathrm{LSV}},\ldots,\bar{g}_I^{\mathrm{LSV}})^T$ consisting of the components $\bar{g}_i^{\mathrm{LSV}}$ (where superscript T denotes transpose). We denote by q another vector that also has I components, i.e., $q = (q_1,\ldots,q_I)^T$. It is clear that a finite number of measurements alone is not sufficient to determine an unknown function of continuous variables, and further conditions on the function (e.g., smoothness, norm, entropy) are needed to obtain a unique solution. The Moore–Penrose generalized solution (see, e.g., [44] and [45]) is the unique function of minimum norm among those that minimize the norm of the residual vector $||\mathrm{P}f - \bar{g}^{\mathrm{LSV}}||$. It can be shown [44], [45] that the Moore–Penrose generalized solution of the system of linear functionals in (1) can be represented as

$$f_{\mathrm{MP}}(x,y,z) = \sum_{i=1}^{I} q_i\, h_i(x,y,z)\,. \tag{7}$$

The right-hand side of (7) represents the adjoint of the operator P applied to the vector q. The coefficients q_i are deter-

mined from (1) as follows. In (1), we replace $f(x,y,z)$ by $f_{\mathrm{MP}}(x,y,z)$ to obtain

$$\bar{g}_i^{\mathrm{LSV}} = \iiint_{\Omega} \left(\sum_{j=1}^{I} q_j \, h_j(x,y,z) \right) h_i(x,y,z) \, dx \, dy \, dz \tag{8}$$

which may be written as

$$\bar{g}^{\mathrm{LSV}} = \mathrm{H} \, q \tag{9}$$

where H is the Gram matrix [21], [44]–[46] with elements

$$\mathrm{H}_{i,j} = \iiint_{\Omega} h_i(x,y,z) \, h_j(x,y,z) \, dx \, dy \, dz \, . \tag{10}$$

The major problem with this method is the need to construct and to solve the large, nonsparse, linear system in (9), given an estimate of $\bar{g}^{\mathrm{LSV}}$ from the measured data, in order to obtain the vector q. For realistic models, the calculation of the matrix elements $\mathrm{H}_{i,j}$ is not a trivial task, particularly in SPECT where the attenuation and the detector response are highly dependent on the location of the emission. For 3-D geometries, and for 3-D SPECT in particular, this approach requires an excessive amount of computation, compared to other methods of image reconstruction from 3-D data. The matrix H of the linear system in (9) is very large ($I \times I$, where I is the number of measurements) and it is also dense (relatively few elements are zero), because the functions $h_i(x,y,z)$ are not localized. These functions are the basis functions that are superimposed to form the image, as shown in (7). The approach described in Section V uses localized basis functions to form the image, leading to a sparse system matrix.

A. Notes and References

Reconstruction methods using image basis functions that are the same as the integration kernels of the measurement process in tomography were formulated independently by at least four groups [47]–[50]. These basis functions were named "natural pixels" [50] and their use by linear reconstruction methods has a solid foundation in the theory of linear inverse problems with discrete data; see, e.g., [21], [44]–[46]. This linear inversion approach is quite general, as demonstrated by a recent application in MRI [20], but most developments have been directed toward reconstruction in SPECT, e.g., [51]–[54], with some also in PET [55], [56].

A nonlinear reconstruction method [47] has also been formulated, and is widely used in some nonmedical applications of tomographic imaging where only a small number of measurements are available. This method is based on a D-C model with uniform strip functions as the integration kernels, and the solution is defined as the function having maximum entropy among those that satisfy the data constraints. This leads to a nonnegative image f for which $(1 + \log f)$ is composed of a sum of strip functions whose coefficients are determined by solving a nonlinear system of equations using an iterative algorithm. A similar approach [48] applied to various optimization criteria for the image function leads to a variety of linear and nonlinear reconstruction methods. We note that several other image reconstruction approaches involving the maximum entropy criterion (but not based on a D-C model) were described in the literature prior to [47], where the earliest appears to be [57].

Image basis functions known as "ridge functions" appear in the theory of image reconstruction from continuous line integral projections at discrete angles, where the projection at each angle is given as a function of the continuous variable in the direction perpendicular to the lines, e.g., [58] and [59]. In this abstract setting where the projections are functions, one can also formulate [44], [60]–[62] an iterative process within a space of image functions that operates on one projection at a time and does not introduce any new structure into the image along the direction of integration for this projection.

V. Image Reconstruction Approach Based on D-D Model

This approach begins by representing the function $f(x,y,z)$ by a finite series expansion involving a chosen set of basis functions. We denote by $\tilde{f}(x,y,z)$ the approximation to $f(x,y,z)$ generated by the linear combination of a finite number J of basis functions, where we denote the jth basis function by $b_j(x,y,z)$ and we denote by $\tilde{f}_j$ the coefficient that multiplies this basis function, so that

$$\tilde{f}(x,y,z) = \sum_{j=1}^{J} \tilde{f}_j \, b_j(x,y,z) \, . \tag{11}$$

When $\tilde{f}(x,y,z)$ is substituted for $f(x,y,z)$ in the D-C expression (1) for $\bar{g}_i^{\mathrm{LSV}}$ we obtain the corresponding D-D model of the physics of the data collection process, with

$$\tilde{g}_i^{\mathrm{LSV}} = \sum_{j=1}^{J} a_{i,j} \, \tilde{f}_j \qquad i = 1, \ldots, I \tag{12}$$

where

$$a_{i,j} = \iiint_{\Omega} h_i(x,y,z) \, b_j(x,y,z) \, dx \, dy \, dz \tag{13}$$

is the contribution of the jth basis function to the ith measurement.

We denote by A the matrix composed of the elements $a_{i,j}$. We denote by g the column vector $(g_1, \ldots, g_I)^T$ consisting of the components g_i (where superscript T denotes transpose), and we denote by $\tilde{f}$ the column vector $(\tilde{f}_1, \ldots, \tilde{f}_J)^T$ (in order to distinguish the vector $\tilde{f}$ from the function $\tilde{f}$, from now on we write all functions with their variables stated explicitly). The D-D expression (12) for $\tilde{g}_i^{\mathrm{LSV}}$ may be written in matrix-vector form as

$$\tilde{g}^{\mathrm{LSV}} = \mathrm{A} \, \tilde{f} \, . \tag{14}$$

The basic task of the reconstruction process is to find a vector $\tilde{f}$ of basis function coefficients such that the vector $\tilde{g}^{\mathrm{LSV}}$ is close (according to some chosen measure) to the corresponding constituent $\bar{g}^{\mathrm{LSV}}$ of the data vector [see (2) and (4))]. In order to do this, we need to have estimates $\tilde{g}_i^{\mathrm{R}}$ and $\tilde{g}_i^{\mathrm{S}}$ of the random coincidence contribution $\bar{g}_i^{\mathrm{R}}$ and the scatter

contribution $\bar{g}_i^{\mathrm{S}}$ to $\mathrm{E}[g_i^{\mathrm{PET}}]$, which is the expected value of the ith measurement (omitting the random term in the case of g_i^{SPECT}). Then, from (2) and (4), the specific task of the reconstruction process is to find a vector $\tilde{f}$ of basis function coefficients such that the vector $(\tilde{g}^{\mathrm{LSV}} + \tilde{g}^{\mathrm{R}} + \tilde{g}^{\mathrm{S}})$, which is the estimate of the mean of the data given $\tilde{f}$, is close (according to some chosen measure) to the data vector g^{PET} (or g^{SPECT}). For a Gaussian model of the data statistics with a uniform variance, the square norm of the difference between these vectors, i.e., $||(\mathrm{A}\tilde{f}+\tilde{g}^{\mathrm{R}}+\tilde{g}^{\mathrm{S}})-g^{\mathrm{PET}}||$, is a natural measure, leading to the use of an algorithm for least squares estimation in the reconstruction process. For the Poisson model of the data statistics, the Poisson likelihood function is a natural measure, which increases as these vectors become more similar, leading to the use of an algorithm for maximum likelihood estimation in the reconstruction process.

For a given image $\tilde{f}$ and a given vector g of measurements, the likelihood $\Pr(g|\tilde{f})$ is the probability of obtaining a data vector identical to the measurement vector if the measurement process were applied to this image. For a given image, the probability of obtaining an individual measurement is given by the Poisson probability with the mean given by the model of the measurement process. The probability of obtaining the measurement vector from the given image, i.e., the likelihood $\Pr(g|\tilde{f})$, is the product of the probabilities for the individual measurements (assuming independent measurements). For the derivation of practical algorithms, it is convenient to maximize the logarithm of the likelihood, rather than the likelihood itself. Taking the logarithm of $\Pr(g|\tilde{f})$ results in a sum of terms, some of which are independent of $\tilde{f}$ and may therefore be omitted from the cost function to be maximized. This cost function is known as the log likelihood, which we denote by $L(\tilde{f}, g)$.

When the data are very noisy, as is frequently the case in emission tomography, the use of the maximum likelihood (ML) or the least-squares (LS) criterion alone leads to images that fit the detailed structure of the data too closely, so the images are excessively noisy. These data fitting criteria need to be augmented by a regularization term, which we denote by $R(\tilde{f})$, that penalizes image roughness or penalizes significant deviations from a given image model or image prior. The algorithm for regularized image reconstruction finds the coefficients $\tilde{f}$ that optimize the penalized log likelihood $L(\tilde{f}, g) - \beta R(\tilde{f})$, or the penalized square norm of the residual vector, where the parameter β determines the relative weight of the two terms.

Image reconstruction approaches based on the D-D model consist of five general components [26], [63]. Within each of these general components, a specific option to be implemented must be selected from a wide array of possibilities. The five general components are as follows.

1) **A set of basis functions,** which enables the image to be represented by a finite number of parameters—There are two different kinds of basis functions, namely, localized and global. The prime example of a localized basis function is the voxel, for which the basis function has unit value inside a small cube and has zero value outside. Global basis functions, such as the basis functions of a Fourier series expansion, make contributions over the whole image region.
2) **A model of the physics of the measurement process**—The LSV model described in Section III is such a model, which involves specifying the measurement kernel $h_i(x, y, z)$. The integration kernel $h_i(x, y, z)$ includes the radiometric sensitivity factor for detection of photons originating from the point (x, y, z), and it includes the effect of photon attenuation, which is described in Sections VI-C and VII.
3) **A model of the measurement uncertainty,** i.e., a model of the probability distribution of each measurement around its expectation value—The Poisson distribution is such a model, as incorporated into the expressions for g_i^{PET} and g_i^{SPECT} in (3)–(6).
4) **An objective function**—This function consists of a data fitting criterion and an image property criterion, and gives a measure of how well an image fits the data and how well this image matches the desired image properties. We denote the objective function by $\Phi(\tilde{f}, g)$. For the case of penalized log likelihood, we have

$$\Phi(\tilde{f}, g) = L(\tilde{f}, g) - \beta R(\tilde{f}) \tag{15}$$

where β is a parameter that controls the balance between the data fitting criterion and the image property criterion, and thereby controls the tradeoff between spatial resolution and noise in the reconstructed image.
5) **A numerical algorithm** to produce the values of the coefficients of the basis functions chosen in category (1), given the measured data and driven by the choices made in categories (2), (3), and (4)—The numerical algorithm is designed to find the image vector for which the objective function is at its maximum (or minimum). When the data set is relatively small and a simple objective function is chosen in (4), it may be feasible to use a noniterative algorithm. However, in most cases a noniterative algorithm does not exist, or it would require a nonfeasible amount of computation. In most cases, image reconstruction based on a D-D model requires the use of an iterative algorithm that produces successive estimates of the set of coefficients of the basis functions. The algorithm is designed to produce a sequence of estimates that converges to a solution maximizing (or minimizing) the objective function.

In principle, the choice of the numerical algorithm should be relatively routine, once the other choices have been made, and the final image should be dependent on these choices and not on the choice of the algorithm. In practice, however, it is common to stop an iterative algorithm before the sequence of estimates has converged, in which case different algorithms will lead to different final images. Historically, the choice of numerical algorithm received much emphasis during the development of image reconstruction approaches based on the

D-D model, while not much attention was paid to choices beyond the simplest ones in categories 1)–4). It is now appreciated that the choices made in 1)–4) have a strong influence on the characteristics of the final image, and that the use of better models leads to better reconstructed images.

A. Examples of Image Reconstruction Methods Using ML-EM Approach

We now give specific examples of a reconstruction algorithm for PET using basic choices for the general components 3)–5) listed above. After presenting these examples, we then revisit the general components 1)–5) and describe some of the alternatives that are available for each.

The objective function used in the examples is the log likelihood for the Poisson model, with no regularization term, i.e., (15) with $\beta = 0$. In the examples, the iterative algorithm to find the maximum-likelihood (ML) image uses the statistical optimization strategy known as expectation maximization (EM) applied to the log likelihood for the Poisson model.

The EM strategy is a general-purpose procedure for the iterative computation of ML estimates, where the update to the current estimate consists of two steps—the expectation step (E) and the maximization step (M). The general formulation of the approach, together with the EM name, appeared in a much-cited paper [64], although many specific applications of the underlying principles had been described previously in the statistical literature. There is now a book [65] on this topic, and a recent book [66] gives a broader view of the place of the EM approach in the statistical literature. The EM procedure for computing ML estimates was introduced into medical imaging in [67]–[69] and has been widely used since that time.

We denote by $\tilde{f}^{(k)}$ the estimate of the image produced by image update k. Given the current estimate $\tilde{f}^{(k)}$, we need to compute the "forward projection" $\mathrm{A}\tilde{f}^{(k)}$, where

$$(\mathrm{A}\tilde{f}^{(k)})_i = \sum_{j=1}^{J} a_{i,j}\, \tilde{f}_j^{(k)} \qquad i = 1, \ldots, I\,. \tag{16}$$

The ML-EM algorithm produces the new estimate $\tilde{f}^{(k+1)}$ from the current estimate $\tilde{f}^{(k)}$ as follows. For $j = 1, \ldots, J$,

$$\tilde{f}_j^{(k+1)} = \tilde{f}_j^{(k)} \frac{1}{\left(\sum\limits_{i=1}^{I} a_{i,j}\right)} \sum_{i=1}^{I} \frac{g_i^{\mathrm{PET}}}{(\mathrm{A}\tilde{f}^{(k)})_i + \tilde{g}_i^{\mathrm{R}} + \tilde{g}_i^{\mathrm{S}}}\, a_{i,j}\,. \tag{17}$$

Although this algorithm is well-justified for the model we have described, the algorithm in (17) is not commonly used in practice in this specific form. One reason is that the sequence of estimates $\tilde{f}^{(k)}$ produced by this algorithm converges at a very slow rate. Much computation is required to get to an acceptable solution, since each new estimate requires a complete cycle through the entire data set. In practice, it is now common to partition the data set into subsets and to use versions of this algorithm that operate on one subset at a time (but not in the natural order of the subsets) to produce a new estimate $\tilde{f}^{(k+1)}$ for each subset processed. These modified forms of the ML-EM algorithm are known as "ordered subset" or "block iterative" methods [70], [71] and the limiting case [72]–[74] uses subsets that each contain only a single measurement, so that the image is updated after the processing of each individual measurement. After only one or two cycles through the data set (i.e., one or two "iterations"), it is typical for these methods to achieve essentially the same result as the ML-EM algorithm achieves after ten or 20 iterations, although mathematical proof of convergence exists for only some of the fast methods.

Another reason for using a modified version of the algorithm in (17) is that many of the currently available PET scanners perform online subtraction of counts obtained as samples from the distribution of random coincidences. We denote by $g_i^{\mathrm{PET-RC}}$ the PET measurement with online randoms correction. This randoms correction decreases the mean and increases the variance, so the distribution of the randoms-subtracted data is no longer Poisson. The consequences for the noise model are described in more detail below. In practice, the algorithm is frequently run on data from which an estimate of the scatter has also been subtracted, so that $(g_i^{\mathrm{PET-RC}} - \tilde{g}_i^{\mathrm{S}})$ is used in place of g_i^{PET} in the numerator of (17), and $(\mathrm{A}\tilde{f}^{(k)})_i$ alone is used in the denominator. In this case, the data are not consistent with the Poisson model on which the algorithm is based, but this algorithm is very robust and is still capable of generating reasonable results.

We now discuss the randoms correction in more detail, since it illustrates the problem of matching the algorithm to the statistics of the data. All PET scanners have a timing window to identify coincident photons, and many current scanners also have a timing window that is delayed relative to the primary window. The output from the primary window contains not only true and scatter coincidences that result from the same annihilation, but also random coincidences where each photon comes from a different annihilation. If a photon is detected within the delayed window, that photon could not have come from the same annihilation that triggered the primary window, so the delayed window provides samples from the distribution of random coincidences. Preferably, the counts of the randoms from the delayed window would be accumulated and stored in the same way as the coincidences (trues+randoms+scatter) from the primary window, which would provide an estimate $\tilde{g}_i^{\mathrm{R}}$ of the mean $\bar{g}_i^{\mathrm{R}}$ of the randoms contribution to the coincidence data for later use by the reconstruction algorithm. However, as noted above, many current scanners perform an online subtraction of the counts of the randoms. This operation is a subtraction of one Poisson variable from another and the variance of a Poisson variable is equal to its mean, so the result is no longer a Poisson variable (since the mean of the result is equal to the difference of the two means and for independent variables the variance of the result is equal to the sum of the two variances). The PET measurement with online randoms correction is denoted by $g_i^{\mathrm{PET-RC}}$, and its mean and variance are given by

$$\mathrm{E}[g_i^{\mathrm{PET-RC}}] = \mathrm{E}[g_i^{\mathrm{PET}}] - \bar{g}_i^{\mathrm{R}} \tag{18}$$

$$\mathrm{Var}[g_i^{\mathrm{PET-RC}}] = \mathrm{Var}[g_i^{\mathrm{PET}}] + \bar{g}_i^{\mathrm{R}} \tag{19}$$

$$= \mathrm{E}[g_i^{\mathrm{PET-RC}}] + 2\,\bar{g}_i^{\mathrm{R}}\,. \tag{20}$$

It has been shown [75]–[77] that an additive offset of $2\,\bar{g}_i^{\mathrm{R}}$ can be applied to the randoms-subtracted data such that the distribution of the offset data is approximated well by a shifted-Poisson model which has the same mean and variance as this distribution. For this model, the corresponding log likelihood and the corresponding ML-EM algorithm (or some other algorithm) can be formulated, leading to a reconstruction method that incorporates a model of the statistical distribution of the data. When randoms correction is done online, the counts of the randoms from the delayed window are not available, and less direct methods [63], [78] must be used to obtain an estimate $\tilde{g}_i^{\mathrm{R}}$ of the mean $\bar{g}_i^{\mathrm{R}}$ of the randoms contribution to the coincidence data for use by the reconstruction algorithm.

We show as an example the modified version of the ML-EM algorithm of (17) for ordered subsets and for randoms-corrected PET data [78]. For $j = 1, \ldots, J$,

$$\tilde{f}_j^{(k+1)} = \tilde{f}_j^{(k)} \frac{1}{\sum\limits_{i \in S(k)} a_{i,j}} \sum_{i \in S(k)} \frac{g_i^{\mathrm{PET-RC}} + 2\,\tilde{g}_i^{\mathrm{R}}}{(\mathrm{A}\tilde{f}^{(k)})_i + 2\,\tilde{g}_i^{\mathrm{R}} + \tilde{g}_i^{\mathrm{S}}}\, a_{i,j} \tag{21}$$

where $S(k)$ is the subset of the data being used for the kth update of the image.

B. Some Design Options for Image Reconstruction Methods

We now revisit the general components 1)–5) and describe some of the alternatives that are available for each. These general components and some of their associated options are:

1) **A set of basis functions,** which enables the image to be represented by a finite number of parameters—The prime example of a localized basis function is the voxel, for which the basis function has unit value inside a small cube and has zero value outside. We have investigated alternative basis functions, known as "blobs," that have spherical symmetry and bell-shaped radial profiles [74], [79]–[82]. Blobs are localized, but are also smooth (almost bandlimited) functions. The represented image is also a smooth function, since it is composed of the superposition of blobs arranged on a grid in 3-D space. The coefficients of the blobs are determined by the reconstruction algorithm, which is therefore searching in a space of smooth functions for a represented image whose model data is a good fit to the measured data. In this way, a global smoothness property of the image is being achieved through the use of these basis functions, instead of by incorporating such a constraint into the objective function.
2) **A model of the physics of the measurement process**—The LSV model described in Section III is such a model, which involves specifying the measurement kernel $h_i(x, y, z)$. The size of the reconstruction problem makes it impossible to store the complete matrix A (except for relatively small two–dimensional (2-D) problems). One approach is to compute the elements $a_{i,j}$ as they are needed. This approach is best suited to fairly simple models. Another approach is to represent the matrix A as the product of several matrices, each of which corresponds to a component of the physical model. The most complete formulation and implementation of this approach for PET has been done by Leahy, Qi, and colleagues [23], [78], [83], [84], where the matrix is factored as

$$\mathrm{A} = \mathrm{P}_{\mathrm{det.sens}}\,\mathrm{P}_{\mathrm{det.blur}}\,\mathrm{P}_{\mathrm{attn}}\,\mathrm{P}_{\mathrm{geom}}\,\mathrm{P}_{\mathrm{positron}}\,. \tag{22}$$

Here, we only indicate the role of each matrix, since full descriptions of these matrices are given in the references. The matrices represent models of the positron travel from the radioactive decay to the annihilation, the geometrical mapping between each image basis function and each pair of detector elements (with no attenuation), the attenuation that modifies the geometrical mapping, the detector blurring introduced by the physical processes within the detector, and the detector sensitivity.

In the case of SPECT, a similar amount of research and development effort has gone into the modeling of the spatially variant detector response and the attenuation of the photons; see, e.g., [14]–[16], [24], [25], [85]. The modeling of attenuation in PET is much simpler than it is in SPECT, as described in Sections VI-C and VII. In both PET and SPECT, much effort has also gone into methods for estimating the scatter contribution to the data. This is a field in itself, with its own specialized methods, which we do not describe further in this paper.

3) **A model of the measurement uncertainty,** i.e., a model of the probability distribution of each measurement around its expectation value—The Poisson distribution is a good model for the number of photons reaching a specific detector element within a specific interval of time. However, the probability distribution of each measurement may be changed significantly by processing operations on the data. One example of such an operation is the online subtraction of random coincidences, and further operations such as normalization and interpolation are routinely performed on the data in practical scanners. An example in [86] of the effect of interpolation on the variance shows a strong spatial pattern of higher and lower values in the variance map of the interpolated data.

   In general, each element of the data vector that is supplied to the reconstruction algorithm does not have a simple probability distribution, such as Poisson or Gaussian. However, as described in [87], it is possible to apply an additive offset or a multiplicative scale factor to each data element so that its distribution is approximately Poisson, in the sense that the mean and variance of the modified data element match those of the Poisson distribution. This approach enables algorithms that are based on the assumption of Poisson statistics to be used with data that is non-Poisson as a result of previous processing operations.
4) **An objective function**—The objective function $\Phi(\tilde{f}, g)$ in (15) for the penalized log likelihood, and

the similar objective function for the penalized least squares criterion, both contain a roughness penalty term $R(\tilde{f})$. The general purpose of this regularization term is to impose a smoothness constraint on the reconstructed image, and the specific form of this term in PET and SPECT is often motivated by the assumption that the spatial distribution being imaged consists of distinct uniform regions with sharp boundaries between them. The design of this term is a challenging task, since it involves not only encouraging local smoothness within uniform regions of the image but also avoiding blurring of their boundaries. A typical roughness penalty is

$$R(\tilde{f}) = \frac{1}{2}\sum_{j=1}^{J}\sum_{k\in N_j} w_{j,k}\,\Psi(\tilde{f}_j, \tilde{f}_k) \tag{23}$$

where N_j is the set of voxels in a defined neighborhood of voxel j, and $w_{j,k}$ are factors that give more weight to voxels in N_j nearer to voxel j compared to those further away. The function $\Psi(\tilde{f}_j, \tilde{f}_k)$ is a penalty function whose value increases as the difference between the values increases for a pair of voxels. The relative difference between the voxel values may be used [88] but it is more common to use the absolute difference, in which case the penalty function reduces to a function of one variable, denoted here by $\psi(t)$, with $\Psi(\tilde{f}_j, \tilde{f}_k) = \psi(\tilde{f}_j - \tilde{f}_k)$. The choice of a basic quadratic function for $\psi(t)$ makes it relatively simple to optimize the objective function $\Phi(\tilde{f}, g) = L(\tilde{f}, g) - \beta R(\tilde{f})$, but results in over-smooth images. A number of modified quadratic functions and other functions for $\psi(t)$ have been investigated that allow the formation of edges by reducing the rate of increase of the penalty function (or by tapering off to a constant value) above a specified value of t (see, e.g., [23], [89]). Functions of this kind have been studied extensively in the field of robust statistics.

The same objective function $\Phi(\tilde{f}, g)$ may be obtained from a Bayesian formulation where the image prior is given by the Gibbs distribution proportional to $\exp(-\beta R(\tilde{f}))$, and the posterior density is the product of the likelihood function $\Pr(g|\tilde{f})$ and the image prior (and divided by $\Pr(g)$, which is independent of $\tilde{f}$). The objective function $\Phi(\tilde{f}, g)$ is obtained by taking the log of the posterior density (and omitting terms that are independent of $\tilde{f}$). The maximum *a posteriori* (MAP) estimate is obtained by finding the image $\tilde{f}$ that maximizes $\Phi(\tilde{f}, g)$. The paper [23] gives a detailed description of this approach and of the functions $R(\tilde{f})$ that have been investigated. Image models relevant to this approach are reviewed in [90], and reconstruction approaches using other kinds of image priors are discussed in [91] and [92].

5) **A numerical algorithm** to produce the values of the coefficients of the basis functions chosen in category 1), given the measured data and driven by the choices made in categories 2)–4)—The numerical algorithm is designed to find the image vector for which the objective function is at its maximum (or minimum). As the objective functions incorporate more complex models of the image, it becomes more difficult to derive special-purpose algorithms and it becomes more attractive to use general-purpose optimization methods. One popular class of methods involves gradient ascent, using preconditioners combined with the conjugate gradient approach [84], [93]–[96]. Reference [78] compares two algorithms for objective functions that incorporate the statistical model of randoms-subtracted data. One algorithm is that of (21), which optimizes an objective function that does not include image properties, and a second algorithm optimizes an objective function that incorporates image properties in the form of a Gibbs distribution.

C. Image Reconstruction From List-Mode Data

We mention briefly another class of algorithms designed for a different format of the data, since this data format and its associated algorithms have been receiving increasing attention in recent years. For the methods described in the other sections of the paper, the data space is partitioned into I bins where, in the PET case, I is (at most) the number of pairs of opposing detector elements and, in the SPECT case, I is (at most) the number of detector elements on the gamma camera (or cameras) multiplied by the number of camera positions around the patient. In the conventional format for the data, the individual counts are accumulated in this set of bins to form a histogram in the data space.

In the practical situation in PET, the number I of histogram bins is usually much smaller than the number of pairs of opposing detector elements, which is 75–200 million for typical clinical scanners (and is much larger than this for some research scanners). It would not be efficient to store and process this number of histogram bins, since the number of measured coincidences is usually much smaller than this, typically, 20–50 million. However, the use of a smaller number of histogram bins results in some loss of spatial resolution, since the counts associated with a number of neighboring lines in space that are individually resolvable by the detector system will be accumulated together in the same histogram bin.

In the more basic format for the data, known as "list mode," the detector coordinates of each individual count are stored sequentially in a long list as the photons are detected. List-mode data can be binned into the histogram format at any time after data collection, then reconstructed by conventional algorithms, or reconstruction can be done directly from the list-mode data, as summarized in this subsection. Historically, the use of list mode has been mainly associated with PET, although there have been recent developments specifically for SPECT [97], [98] and for reconstruction from Compton-scatter data [99]. We focus here on the use of list-mode data in PET.

There is only a limited choice of algorithms for image reconstruction from list-mode data in PET, in contrast to the

wide variety for data in the conventional histogram format. The problem of reconstruction from list-mode data lends itself naturally to an ML formulation and subsequently to algorithms for estimating the ML solution given list-mode data [100]–[107]. Alternatively, the well-known ML-EM algorithm for binned PET data that uses the EM strategy can be decomposed into operations on the individual events [108]–[113]. This simple alternative derivation in fact leads to the same algorithm as that derived more rigorously by applying the EM strategy to the ML formulation specifically for list-mode data (except for the algorithm of [101], which employs a partitioning of the data space). The algorithm described in [113] is being used in one of the commercial PET scanners using a rotating pair of gamma cameras [114], [115]. These list-mode approaches derived from the ML formulation involve the same five D-D components (but for different data) as those for the conventional approaches, namely, image basis functions, model of the measurement physics, model of the measurement statistics, objective function with a log-likelihood term and possibly a penalty term, and numerical algorithm. Another approach to reconstruction from list-mode data involves event-by-event backprojection, followed by spatially-variant filtering or by iterative refinement of the image. Algorithms based on this approach have been investigated for many years—a recent example is found in [116] and [117].

Although the focus of this paper is on reconstruction methods for static imaging, we note that list-mode data is advantageous for dynamic imaging, since the time of the event (and indeed any other measurable parameter) can be recorded for each photon pair. For dynamic studies using list-mode data, one possibility is to pursue a hybrid approach to processing in which the time variable is continuous and partitioning of the space is used for the geometric variables, as described in [118], [119].

D. Notes and References

The general features and some specific examples of the image reconstruction approach based on the D-D model are described in [63] and [120], and further in [121, Ch. 10] and [26]. Surveys of the methods used in PET include [22] and [23], and [122] gives an overview for PET and SPECT. There is much research activity at present on the topic of iterative algorithms, involving a wide variety of methods, as summarized in [123]. Non-iterative algorithms have also been investigated for SPECT [124] and PET [125], although their use is limited to 2-D applications at present because of their computational demands. Iterative algorithms also have large computational demands, especially when used with the data sets produced by the current generation of high resolution PET scanners, and work is underway to implement these algorithms on clusters of commodity PC processors [84], [126].

The topic of this section concerns methods based on D-D models for the problem of reconstructing emission maps from the emission data in PET and SPECT. A closely related problem in PET and SPECT is the reconstruction of attenuation maps from transmission data obtained using an external source of radiation that transmits photons through the body to the detector, as outlined in Section VII. The concepts and algorithms for the transmission problem are described in detail in [127], and these have much in common with the methods for emission data.

The current work on reconstruction methods for PET and SPECT emphasizes the optimization of objective functions that are based on statistical models of the measurement process. However, much work on reconstruction methods has also resulted from considering algorithms for finding a solution to an inconsistent system of equations (or inequalities), where each measurement may be weighted according to an estimate of its variance. Such methods are not optimal for low-count data, where the probability distribution of each measurement is not symmetric around its expectation value. However, such methods can produce useful results in many practical applications, and iterative reconstruction algorithms of this kind have been used since the earliest days of computed tomography, including the original 1971 EMI CT scanner. As early as 1974, review papers [128]–[130] were classifying such algorithms, including ones for weighted least squares reconstruction, which is still an important option today. A general formulation [62] includes as special cases many previously published algorithms, and another significant paper [131] describes the use of the conjugate gradient algorithm for computing the weighted least squares solution. Many iterative methods are described and analyzed in the first book on image reconstruction algorithms [132], in the early review paper [120], and in the recent book [121] and review paper [133].

The basic task of seeking a solution of (14) can be interpreted as an instance of the convex feasibility problem, which is an active topic of investigation in the applied mathematics literature; see, e.g., [134]. In that area there is a popular class of methods called "projection methods," where the word projection is meant in the geometric sense of finding a point in a given set, closest to another given point in space (and not in the sense it is used in the title of this paper). The well-known ART algorithm for image reconstruction [132], [133] is such a projection method and the ML-EM algorithm can also be treated as an alternating projections method; see [135] and [136]. In an analogous fashion to the block iterative (ordered subset) versions of the ML-EM algorithm mentioned in Section V-A, the quest for alternative algorithmic structures is also an active topic of investigation for other image reconstruction methods; see, e.g., [137] and [138], and for more general projection methods, e.g., [139].

VI. Image Reconstruction Approach Based on C-C Model

This approach begins by obtaining a C-C model from the D-C expression (1) for $\bar{g}_i^{\mathrm{LSV}}$ by interpreting this component of the measurement vector as being a sample of a continuous function in the measurement space. The next step is to make simplifications to the model of the measurement process until we obtain a C-C model for which an analytic inversion formula can be derived. This approach leads to fast methods that are widely used in practice, but their performance is certainly

less than optimal since they are linear methods that do not incorporate detailed models of the physics of the measurement process or of the signal-dependent statistics of the measurements that are obtained in emission tomography.

In this paper, we focus on the geometries of data collection that lead to parallel-ray projections, since this particular case is the one of major practical importance in PET and SPECT (and in many other applications, such as electron microscopy). Other data collection geometries that lead to projections composed of nonparallel rays are also found in SPECT, where some applications use converging beam collimators or pinhole apertures, so that the data are collected in the form of fan beam projections or cone beam projections. Similar projections are also produced by the transmission scans in PET and SPECT, as described in Section VII-A, and they are also of major practical importance in X-ray CT; see, e.g., [9] and the papers on X-ray volume imaging in this Special Issue. The derivations of inversion formulas for fan beam and cone beam projections involve specialized topics that are beyond the scope of this paper, in which the description of the C-C approach is directed toward the case of parallel-ray projections.

The first simplification of the C-C approach involves shrinking each of the tube-shaped regions of integration to an infinitely thin line, replacing the 3-D integral over the volume of the tube by a one-dimensional (1-D) integral along the line, and setting the integration kernel $h_i(x,y,z)$ to the same constant value for all points along the line and for all lines $i = 1, \ldots, I$. This simplification approximates the LSV model, not only by a linear spatially invariant (LSI) model, but also by a special case of the LSI model involving integration of $f(x,y,z)$ along lines.

In order to specify the location of a line in 3-D space, we define rotated coordinates (x', y', z'), as illustrated in Fig. 5, where these coordinates result from a rotation of the original coordinates (x,y,z) by an angle ϕ about the z axis, followed by a rotation by an angle θ about the new x axis (so that for $\theta = 0$ the y' axis is in the x-y plane). We define the line in space as being parallel to the y' axis and passing through the point $(x', 0, z')$, so that the line is specified by the four parameters (x', z', ϕ, θ).

We now have the C-C model

$$g^{\mathrm{LSI}}(x', z', \phi, \theta) = \int_L f(x,y,z)\, dy' \tag{24}$$

where (x,y,z) are the coordinates in the fixed system of a point which is on the line of integration L and is specified by (x', y', z') in the rotated coordinates. Here $g^{\mathrm{LSI}}(x', z', \phi, \theta)$ is a continuous function of the variables in the measurement space, and the physical component of the ith measurement is the value of this function at the point $(x_i', z_i', \phi_i, \theta_i)$ in the measurement space.

For a given orientation (ϕ, θ), the function of the remaining two variables (x', z') is known as the parallel ray projection of $f(x,y,z)$, for this direction of the lines of integration. We denote the parallel ray projection by $p_{\phi,\theta}(x', z')$, where

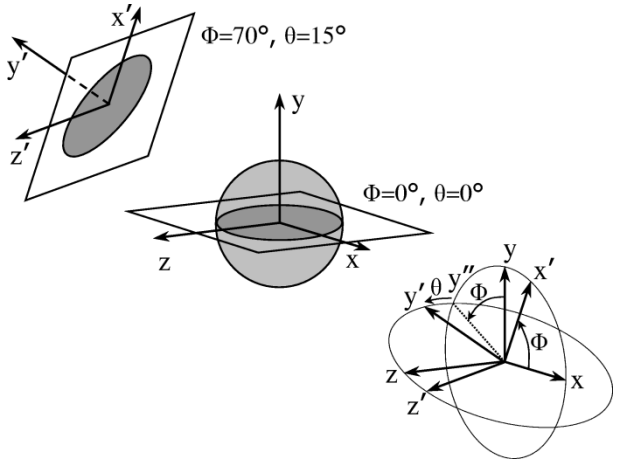

Fig. 5. Illustration of the projection data coordinates (x', z', ϕ, θ) with respect to the 3-D coordinate system (x, y, z) of the scanner. Projection integration is done in the y' direction of the rotated coordinate sytem (x', y', z') (illustrated on the right). The original coordinate system (x, y, z) is first rotated around the z axis by the angle ϕ (the (x, y) plane is rotated to get the new x' and preliminary y'' axes). In the second step, the coordinate system is further rotated around the new x' axis by the angle θ (the (y'', z) plane is rotated to get the final y' and z' axes). For the case of $\phi = 0^\circ$ and $\theta = 0^\circ$, the x' and z' projection coordinates are equivalent to the image x and z coordinates (center illustration). The orientation of the projection coordinate system for $\phi = 70^\circ$ and $\theta = 15^\circ$ is illustrated at the left (note that the y' axis is oriented away from us in this example).

$$p_{\phi,\theta}(x', z') = g^{\mathrm{LSI}}(x', z', \phi, \theta)\,. \tag{25}$$

For parallel ray projections, there is a simple relationship [140] between the 2-D Fourier transform of each parallel ray projection and a corresponding plane within the 3-D Fourier transform of the function $f(x,y,z)$. This relationship is known by various names, including Fourier projection theorem, Fourier central section theorem, and projection slice theorem. We demonstrate this relationship for the special case where $\phi = 0$ and $\theta = 0$, so that $(x', y', z') = (x, y, z)$, and then infer the general case from the well-known property that rotation of a function corresponds to rotation of its Fourier transform [141], [142]. We denote by $(\omega_x, \omega_y, \omega_z)$ the Fourier space variables corresponding to (x, y, z). We denote by $\hat{f}(\omega_x, \omega_y, \omega_z)$ the function that is the 3-D Fourier transform of $f(x,y,z)$, and we denote by $\hat{p}_{\phi,\theta}(\omega_{x'}, \omega_{z'})$ the function that is the 2-D Fourier transform of $p_{\phi,\theta}(x', z')$. We define the Fourier transforms of $f(x,y,z)$ and $p_{\phi,\theta}(x', z')$ by

$$\hat{f}(\omega_x, \omega_y, \omega_z) = \iiint_\Omega f(x,y,z)\, e^{-i(\omega_x x + \omega_y y + \omega_z z)}\, dx\, dy\, dz \tag{26}$$

$$\hat{p}_{\phi,\theta}(\omega_{x'}, \omega_{z'}) = \iint_\Omega p_{\phi,\theta}(x', z')\, e^{-i(\omega_{x'} x' + \omega_{z'} z')}\, dx'\, dz'\,. \tag{27}$$

We now consider the values of the 3-D Fourier transform of $f(x,y,z)$ on the 2-D plane $\omega_y = 0$ through the origin of the 3-D Fourier space, which are

$$\begin{aligned}\hat{f}(\omega_x, 0, \omega_z) &= \int\int\int_{\Omega} f(x,y,z)\, e^{-i(\omega_x x + \omega_z z)}\, dx\, dy\, dz \\ &= \int\int \left[\int_{\Omega} f(x,y,z)\, dy\right] e^{-i(\omega_x x + \omega_z z)}\, dx\, dz \\ &= \int\int_{\Omega} p_{\phi=0,\,\theta=0}(x,z)\, e^{-i(\omega_x x + \omega_z z)}\, dx\, dz \\ &= \hat{p}_{\phi=0,\,\theta=0}(\omega_x, \omega_z)\,. \end{aligned} \tag{28}$$

The final expression is simply the 2-D Fourier transform of the parallel ray projection at the orientation $\phi = 0$, $\theta = 0$, for which the lines of integration are perpendicular to the plane $y = 0$. The general case of a parallel-ray projection at an arbitrary orientation corresponds to the $\phi = 0$, $\theta = 0$ projection of a rotated version of the object, whose Fourier transform is a similarly rotated version of the Fourier transform of the original object. The relationship therefore exists in the general case, where the 2-D Fourier transform of a parallel-ray projection at a specific orientation (ϕ, θ) is equal to the values of the 3-D Fourier transform on the 2-D plane $\omega_{y'} = 0$ through the origin having the corresponding specific orientation (i.e., perpendicular to the lines of integration). The statement of the Fourier central section theorem is, therefore, expressed as

$$\hat{p}_{\phi,\theta}(\omega_{x'}, \omega_{z'}) = \hat{f}(\omega_x, \omega_y, \omega_z)\Big|_{\omega_{y'}=0}\,. \tag{29}$$

We now use the inverse Fourier transform to express $f(x,y,z)$ in terms of $\hat{f}(\omega_x, \omega_y, \omega_z)$, which in turn is expressed in terms of $\hat{p}_{\phi,\theta}(\omega_{x'}, \omega_{z'})$ using the Fourier central section theorem as follows:

$$\begin{aligned} f(x,y,z) &= \frac{1}{(2\pi)^3} \int_{-\infty}^{\infty}\int_{-\infty}^{\infty}\int_{-\infty}^{\infty} \hat{f}(\omega_x, \omega_y, \omega_z) \\ &\quad \times e^{i(\omega_x x + \omega_y y + \omega_z z)} d\omega_x d\omega_y d\omega_z \end{aligned} \tag{30}$$

$$\begin{aligned} &= \frac{1}{(2\pi)^3} \int_{-\infty}^{\infty}\int_{-\infty}^{\infty}\int_{-\infty}^{\infty} \hat{p}_{\phi^*,\theta^*}(\omega^*_{x'}, \omega^*_{z'}) \\ &\quad \times e^{i(\omega_x x + \omega_y y + \omega_z z)} d\omega_x d\omega_y d\omega_z \end{aligned} \tag{31}$$

where $\omega^*_{x'}$, $\omega^*_{z'}$ are the rotated coordinates of $(\omega_x, \omega_y, \omega_z)$ on one of the planes (of the set of planes) containing both the Fourier space origin and $(\omega_x, \omega_y, \omega_z)$, and where ϕ^* and θ^* are the rotation angles of this plane. Since $\hat{p}_{\phi,\theta}(\omega_{x'}, \omega_{z'})$ is obtainable from the projection $p_{\phi,\theta}(x', z')$ by 2-D Fourier transformation, we now have an inversion formula that is derived from the C-C model, and that expresses $f(x,y,z)$ in terms of its parallel ray projections. The next step in the image reconstruction approach based on the C-C model involves specifying a method for the numerical evaluation of the inversion formula in order to produce samples $f(x_k, y_k, z_k)$ on a grid of points in image space, using the discrete data. Although this is the simplest example of an inversion formula for 3-D reconstruction, a number of problems arise when we consider using it in the practical application of 3-D reconstruction in PET (or SPECT). We discuss some of these practical issues in the following subsections.

A. Geometry of Data Collection

In the image reconstruction approach based on the C-C model, the geometry of the data collection has a major influence on all aspects of the approach, namely, the model, the inversion formula based on the model, and the numerical evaluation of the inversion formula. Much effort has gone into the development of specific inversion formulas and specific data processing procedures for a wide variety of applications involving image reconstruction from projections. We now outline some of the specific geometrical issues that arise when the approach based on the C-C model is used in PET.

Consideration of the Fourier central section theorem shows that the parallel ray projections corresponding to $\theta = 0$ and to ϕ covering the range $[0, \pi]$ are sufficient to cover Fourier space, and would therefore be sufficient for reconstruction. In this case, the 3-D reconstruction procedure decomposes in the z direction into a separate 2-D reconstruction for each value of z. In PET, the data can be formatted into projections covering a range of oblique angles $[-\theta_{\max}, \theta_{\max}]$. From the geometrical point of view, these projections contain more lines of integration than necessary. Recall that this situation arises in the simplest 3-D inversion formula (31), where the required value of $\hat{f}(\omega_x, \omega_y, \omega_z)$ is available from more than one projection transform plane. In PET, the measurement for each line of integration often consists of only a few photon pairs and, from the statistical point of view, it is important to ensure that geometrically redundant measurements make suitably weighted contributions to the reconstructed image.

Another geometrical issue arises in PET with parallel-ray projections at oblique angles ($\theta \neq 0$) because the cylindrical detector (or pair of planar detectors) cannot measure the parts of the projections near the ends of the range of z', leading to incomplete projections, as illustrated in Fig. 6. However, the typical inversion formulas are derived for complete projections. For example, the complete projection $p_{\phi,\theta}(x', z')$ is needed in order to obtain its Fourier transform $\hat{p}_{\phi,\theta}(\omega_{x'}, \omega_{z'})$. The approach adopted in PET [143], [144] is to first obtain a low-statistics preliminary image from the nonoblique data ($\theta = 0$, or θ in a small range around zero). Line integrals through this reconstructed image are then calculated, and these estimated data are used to fill in the missing parts of the projections. This augmentation of the data set enables an inversion formula that is derived for the spatially invariant case of complete projections to be used for PET, in which the measured projections are incomplete and the process of data collection is spatially variant.

B. Design of Reconstruction Algorithm for Discrete Data

After an inversion formula is derived, the next step involves designing a numerical procedure to evaluate it. This

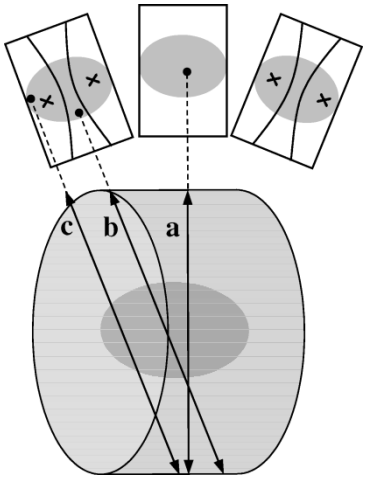

Fig. 6. Illustration of the geometrical configurations of the projection data for photon pairs that do not scatter. *a* represents a photon pair traveling in the nonoblique direction $(\theta = 0)$, i.e., perpendicular to the z axis, which is the axis of the detector cylinder. All nonoblique photon pairs which originate from within the scanner field of view are detected. *b* represents a photon pair traveling in an oblique direction $(\theta \neq 0)$ for which both photons are detected. *c* represents a photon pair traveling in an oblique direction which originated from within the scanner field of view, but for which one of the photons misses the detector cylinder. The projections at oblique directions contain regions, marked by **x** in the diagram, that correspond to oblique lines where one of the photons misses the detector cylinder.

may involve manipulating the formula to obtain a modified version that is theoretically equivalent, but is more suitable for numerical evaluation. This may also involve introducing regularization to provide control over the smoothness properties of the solution and over the noise amplification of the inversion process.

We now consider the numerical evaluation of the inversion formula based on the Fourier central section theorem. The simplest format for the data consists of a Cartesian grid in the variables (x', z') on each projection plane, with equally spaced angles in ϕ over the range [0, π] and equally spaced angles in θ over the range of oblique angles $[-\theta_{\max}, \theta_{\max}]$. If parts of the projection plane are not measured, as is the case in PET, the missing data must be estimated, as described in the previous subsection. The fast Fourier transform (FFT) algorithm applied to the data on a projection plane will produce the values of $\hat{p}_{\phi,\theta}(\omega_{x'}, \omega_{z'})$ on a Cartesian grid in the variables $(\omega_{x'}, \omega_{z'})$. The critical step in the procedure involves using these values to determine the values of $\hat{f}(\omega_x, \omega_y, \omega_z)$ on a 3-D Cartesian grid. Once this is done, using the projection planes at all of the discrete angles, the inverse FFT algorithm applied to the 3-D transform values will produce the values of $f(x, y, z)$ on a 3-D Cartesian grid.

The critical step involves using the available data on a highly nonuniform grid in the 3-D transform space to estimate the required values on a Cartesian grid. It is natural to attempt to estimate these values using a simple interpolation approach but, unfortunately, this leads to poor results, even when oversampling is used (the reasons for this are discussed in, e.g., [145]). Although the concept of using Fourier transforms for image reconstruction from projections was known in the 1950s and 1960s in radio astronomy [140], [146], [147] and in electron microscopy [148]–[150], it is only comparatively recently that the problems of this critical step have been resolved. Instead of using simple interpolation, a method known as "gridding," which originated in the radio astronomy field [151] and was introduced into medical imaging in [152], is used to estimate the required values on the Cartesian grid. Briefly, this involves pre-weighting the data on the nonuniform grid (based on the local density of the available samples), convolving this data with a smooth, almost-bandlimited kernel, sampling the result on the Cartesian grid, and optionally a further post-weighting [153] of the values on this grid. An inverse Fourier transform is then performed from the values on the Cartesian grid to a Cartesian grid in the image space, where the result is weighted to compensate for the Fourier-domain convolution by the interpolation kernel. This approach has been shown to give good results in 2-D X-ray CT [154] and 3-D PET [153], and is used extensively in MRI, e.g., [155], [156].

We now describe an alternative approach that is based on a modified version of the Fourier inversion formula. This approach involves a change of variables in the 3-D inverse Fourier transform, so that polar variables (ω, ϕ, θ) are used instead of $(\omega_x, \omega_y, \omega_z)$, where $\omega = \sqrt{\omega_x^2 + \omega_y^2 + \omega_z^2}$. The 2-D Fourier integral with respect to (x', z') of the projection at angles (ϕ, θ) is then combined with the inverse Fourier integral over the radial variable ω to produce a 2-D convolution of the projection with a filter kernel. The inverse Fourier integral over the angular variables (ϕ, θ) is now simply an image-space superposition of the filtered projections, which is an operation known as "backprojection" of the filtered projections. The values of each filtered projection are known on a 2-D Cartesian grid, and interpolation is required to determine the contribution of this filtered projection to a point in the image (on the 3-D image grid). In this case, a simple interpolation method leads to good results, in contrast to the case of interpolation between values of the Fourier transform of the projection.

This approach leads to the most widely used class of algorithms for discrete data, known as "convolution-backprojection." The 2-D version of convolution-backprojection (reviewed in, e.g., [145]) is a simple and robust algorithm [146], and [157]–[160] that has been widely used since the early 1970s. In the case of 2-D reconstruction, the filter kernel that is convolved with each 1-D projection is the inverse Fourier transform of the function $|\omega_{x'}|W(\omega_{x'})$, where W is a window function that controls the tradeoff between the spatial resolution and the noise amplification in the reconstruction process. In the case of 3-D reconstruction in PET, the specification of the filter kernel is more complex [144], because of the geometrical redundancy of the data and the need to incorporate an appropriate weighting of this data. In the case of 3-D reconstruction in electron microscopy [150], the data sets typically have geometrical insufficiency rather than redundancy (e.g., projections for only a single value of the oblique angle θ), and a filter kernel and weighting have been devised [161] for this data. As in the 2-D case, a multiplicative low-pass window function in Fourier space con-

trols the noise-resolution tradeoff. The 3-D version of convolution-backprojection is widely used in PET [143], [144], where it is known as 3DRP, with the RP denoting the operation of reprojection that is needed to estimate the unmeasured parts of the projections (see Section VI-A and Fig. 6) prior to convolving the projections with the filter kernel.

C. Inversion for C-C Model With Attenuation

The inversion approaches described in the previous sections are based on the simplest C-C model of ECT in which the data are line integrals of the function to be determined. Inversion is also possible for a more realistic C-C model of ECT that incorporates the attenuation of the photons between the point of emission and the detector.

Introducing notation similar to that of [45], L denotes the line of integration, $L(x,y,z)$ denotes the section of L between the point (x,y,z) on L and the detector in the SPECT case, and in the PET case $L_+(x,y,z)$ and $L_-(x,y,z)$ denote the two sections of L between the point (x,y,z) on L and the two opposing detectors. We denote by $\mu(\ell)$ the linear attenuation coefficient at the point ℓ along the line, so that $\exp[-\mu(\ell)\,d\ell]$ is the probability that a photon is successful in traversing a differential element of length $d\ell$ without interaction with the attenuating material.

In SPECT, each radioactive decay produces one photon that travels from the point of decay to the detector and the detector accumulates those photons that are traveling in the direction (ϕ,θ) and that did not interact with the attenuating material on their path to the detector. We denote by $p_{\phi,\theta}^{\mathrm{SPECT}}(x',z')$ the projection at orientation (ϕ,θ) obtained from the C-C model of SPECT with attenuation, which is expressed as

$$p_{\phi,\theta}^{\mathrm{SPECT}}(x',z') = \int_L f(x,y,z)\, e^{-\int_{L(x,y,z)} \mu(\ell)\, d\ell}\, dy' \quad (32)$$

where, as before, (x,y,z) are the coordinates in the fixed system of a point which is on the line of integration L and is specified by (x',y',z') in the rotated coordinates. In practice, some scattered photons are also detected, but this model does not include their contributions to the SPECT data.

In PET, each radioactive decay produces two photons that travel in opposite directions from the point of decay to the opposing two detectors. The detector system records a "true coincidence" count when the two individual photons do not interact with the attenuating material on their respective paths to the detectors, and they are detected at almost the same time (i.e., within a short time window, typically 6–12 ns). In practice, some scattered photons are also detected, and sometimes two photons originating from two different radioactive decays are detected within the time window, known as "random" (or "accidental") coincidences. We now state a C-C model of PET that includes the effect of attenuation, but does not include the contributions of scatter and random coincidences to the PET data. We denote by $p_{\phi,\theta}^{\mathrm{PET}}(x',z')$ the projection at orientation (ϕ,θ) obtained from the C-C model of PET with attenuation, which is expressed as

$$\begin{aligned} p_{\phi,\theta}^{\mathrm{PET}}(x',z') &= \int_L f(x,y,z) e^{-\int_{L_+(x,y,z)} \mu(\ell) d\ell}\, e^{-\int_{L_-(x,y,z)} \mu(\ell) d\ell}\, dy' \\ &= e^{-\int_L \mu(\ell)\, d\ell} \int_L f(x,y,z)\, dy' \\ &= e^{-\int_L \mu(\ell)\, d\ell}\, p_{\phi,\theta}(x',z') \end{aligned} \quad (33)$$

where, as before, (x,y,z) are the coordinates in the fixed system of a point which is on the line of integration L and is specified by (x',y',z') in the rotated coordinates.

Compared to SPECT, the influence of attenuation on the projection data is much simpler in PET, since the detection probability for a decay somewhere along a line does not depend on the location of the decay along the line, but only depends on the integral of attenuation over the whole line. In the case of PET, inversion methods developed for $p_{\phi,\theta}(x',z')$ can be used, after doing a preprocessing operation on the data to correct for the effect of attenuation. Preprocessing operations are discussed in Section VII.

In the case of SPECT, the derivation of an inversion formula from the C-C model with attenuation is a challenging task, even in the 2-D case. A less general form of the model for 2-D SPECT, which leads to a formulation known as the exponential Radon transform, is obtained when the attenuation coefficient can be modeled as constant (of known value) within a region of the (x,y) plane containing the support of the activity distribution. The exponential Radon transform corresponds to (32) with a constant value of μ, and with restriction to $\theta = 0$ and the 2-D slice $z = z' = 0$. Inversion formulas for the exponential Radon transform were obtained in 1979–1980, in the Fourier domain [162], and in the spatial domain [163]. The spatial-domain formula may be implemented as a convolution-backprojection algorithm, where the filter is a modified version of the $|\omega|$ filter, and the filtered projections are backprojected with an exponential weighting factor. Other inversion formulas were obtained independently after 1980. In 1995, it was shown [164], [165] that four inversion formulas for the exponential Radon transform (including those of [162], [163]) can be interpreted as special cases of a broad class of linear methods, and that this generalization includes a new method having better noise properties than the methods known previously.

The model for 2-D SPECT with spatially varying attenuation coefficient, and which is known for all (x,y), leads to a formulation known as the attenuated Radon transform. Inversion of this transform was an open problem until around 2000, when deep analytical insights led to two different derivations of two equivalent inversion formulas [166], [167], and further analysis [45], [168]. Once again, the inversion process has the convolution-backprojection structure, where the data are pre-weighted before the convolution with a specified filter kernel, followed by post-weighting,

after which the filtered projections are backprojected with an exponential weighting factor. References [167], [169], and [170] contain detailed descriptions of the adaptations of the inversion formulas to produce reconstruction algorithms for discrete data, along with some promising results of initial tests. This remarkable algorithm is a significant accomplishment that has elevated the C-C formulation for SPECT from a theoretical concept to a model having practical relevance for SPECT reconstruction.

D. Notes and References

Many of the books already cited contain some description of inversion methods based on the C-C model. Inversion formulas for image reconstruction from various kinds of known projections date back at least as far as the now-famous paper of Radon in 1917. English translations of the original German paper may be found in [171, Appendix A] and in [172] (which contains translator's notes and a list of corrections, and is preceded by a brief biography [173]). A recent paper [174] gives an overview of the historical development of CT and the associated inversion formulas. Early survey papers include [129]–[131], [160], and [175]–[179]. The first comprehensive textbook devoted to image reconstruction algorithms is [132], and the fundamentals of radiological imaging using X-rays and gamma rays are described in detail in [3]. Another early book on image reconstruction methods and applications [171] (reprinted 1993) has an extensive bibliography of the work prior to 1983. Further publications from this era and having broad scope include a review chapter [180] and an extensive bibliography [181]. Tutorial descriptions of the C-C based inversion methods from the point of view of physics and engineering may be found in [8], [144], [145], [182], [183] and a recent concise survey [184] gives references to a selection of key papers, journal special issues, and books. The mathematical foundations of these inversion methods are described in detail, but also in a constructive manner accessible to theoretically inclined physicists and engineers, in [44] and [45]. Another book [185] on the mathematical foundations of these methods gives detailed tutorial descriptions (at the level of advanced undergraduate and beginning graduate students) of a wide range of mathematical topics relevant to the analysis of imaging systems, motivated by examples involving the inversion formulas for 2-D X-ray CT and their discrete implementations. Books directed primarily to mathematicians include [186], [187], and there is an extensive literature in the related branch of mathematics (integral geometry).

VII. Processing of Transmission Data and Emission Data Prior to Emission Reconstruction

A. Processing of Transmission Data to Obtain Map of Attenuation Coefficient

In both PET and SPECT, and for reconstruction methods derived from any of the described approaches (C-C, D-D, D-C), there is a need to obtain an image of the spatial distribution of the attenuation coefficient prior to doing the reconstruction of the emission distribution. This is done by using an external source of radiation that transmits photons through the body of the patient to the detector [188]–[190]. The transmission data are recorded in this situation, and also in the situation when there is no patient in the scanner, and the ratio of these measurements for the ith line gives an estimate of the probability of no interaction with the attenuating material for photons traveling the full length of this line, i.e., the exponential factor $\exp(-\int_L \mu(\ell)\, d\ell)$ in (33). In principle, this estimate could be used directly in PET since the reciprocal of the above ratio gives an estimate of the attenuation correction factor for the data, but the largest correction factors would result from the fewest available counts, leading to very noisy estimates.

Another approach involves taking the logarithm of each such ratio of counts to obtain estimates of the line integrals of the attenuation coefficient distribution, as in X-ray CT, and then reconstructing the distribution from this data using a standard CT algorithm for the transmission geometry. In fact, some recent scanner developments combine a CT scanner with an ECT scanner to form combined CT-SPECT or CT-PET systems [114], [115], [191], [192]. The result of reconstruction from the transmission data can be smoothed, or segmented into discrete regions, to form an attenuation map, e.g., [193], [194]. Using this map, integrals can be calculated for complete lines (PET) or partial lines (SPECT), either for incorporating in the D-D models (PET, SPECT) or for preprocessing the emission data (PET only).

Although this approach using the logarithm of the count data works well when the transmission data sets have large numbers of counts, as is the case with a CT scanner and its X-ray tube source, most PET and SPECT scanners use comparatively weak (low flux) radioactive sources to obtain the transmission measurements, which therefore have only low numbers of counts. In this case, it is far from optimal to take the logarithm of the low-count data to obtain estimates of line integrals, since low-count Poisson data are not symmetric about the mean and contain measurements having zero counts. In practice, the data contain additional contributions from scatter and from the emission activity, which is often present in the patient at the same time as the transmission scan is being done. Estimates of these contributions are often subtracted from the data, which can result in some counts becoming negative, leading to further problems when attempting to take the logarithm. For low-count data, it is preferable to formulate a statistical model of the measurement process and to derive an algorithm that operates directly on the original count data to obtain the attenuation map, e.g., [195]. A recent review [127] provides a comprehensive description of statistical image reconstruction methods for low-count transmission measurements. The formulation of the model and the algorithms that are derived for the transmission problem using this approach have much in common with the corresponding formulation and algorithms for the emission problem.

All methods for the processing of transmission data result in the propagation of noise and measurement errors from the transmission data into the reconstructed map of the attenuation coefficients, and from there into the corrected emission

data or the system matrix of emission reconstruction, and finally into the reconstructed image of the emission activity. The analysis of the propagation of noise and errors from the transmission data is a challenging problem; see, e.g., the analysis and references in [196].

B. Preprocessing of Emission Data to Compensate for Attenuation

In order to use inversion formulas that express the spatial distribution $f(x, y, z)$ in terms of the projections $p_{\phi,\theta}(x', z')$, we first need to estimate, from the measured data, the values of the projections for a discrete set of lines in space. We consider the case of PET, where we have previously introduced the notation g_i^{PET} for the measurement associated with the ith line, and we have denoted by $\tilde{g}_i^{\mathrm{R}}$ and $\tilde{g}_i^{\mathrm{S}}$ the estimates of, respectively, the random coincidence contribution $\bar{g}_i^{\mathrm{R}}$ and the scatter contribution $\bar{g}_i^{\mathrm{S}}$ to the expected value of the ith measurement. We denote by $\tilde{p}_i$ and $\tilde{p}_i^{\mathrm{PET}}$ the estimated values, for the ith line, of $p_{\phi,\theta}(x', z')$ and $p_{\phi,\theta}^{\mathrm{PET}}(x', z')$ in (33). Now $\tilde{p}_i^{\mathrm{PET}}$ may be estimated from the measurement g_i^{PET} using the relationship

$$g_i^{\mathrm{PET}} = \tilde{p}_i^{\mathrm{PET}} + \tilde{g}_i^{\mathrm{R}} + \tilde{g}_i^{\mathrm{S}} \tag{34}$$

which is based on (2), where the measurement g_i^{PET} is used in place of the expected value in that equation, and $\tilde{p}_i^{\mathrm{PET}}$ is the model of PET with attenuation, replacing the corresponding model term $\tilde{g}_i^{\mathrm{LSV}}$. We denote by C_i the attenuation correction factor (ACF) for the ith line, where

$$C_i = \exp\left(+ \int_{L_i} \mu(\ell)\, d\ell \right) . \tag{35}$$

We can now use (33) to express the estimated projection value in terms of the estimated value corresponding to the model of PET with attenuation, and then use (34) to obtain

$$\tilde{p}_i = C_i\, \tilde{p}_i^{\mathrm{PET}} \tag{36}$$

$$= C_i\, \left(g_i^{\mathrm{PET}} - \tilde{g}_i^{\mathrm{R}} - \tilde{g}_i^{\mathrm{S}} \right) . \tag{37}$$

This equation indicates the operations that are necessary to preprocess measured PET data prior to using reconstruction algorithms derived for line integral projections. In practice, the attenuation correction factor C_i is multiplied by a normalization factor (not shown in this equation) that compensates for the nonuniformity of response of different detector elements. This nonuniformity is caused by individual variations in detector efficiencies and by systematic variations resulting from the geometrical arrangement of the detector elements.

The preprocessing of each measurement requires estimates of the normalization factor, the attenuation correction factor, the contribution of random coincidences, and the contribution of scatter coincidences, each of which is a significant problem on its own [197]. Of course, the same estimates are required when using a reconstruction algorithm based on the D-D model, where the derivation of such an algorithm is usually based on an assumption that the data are distributed according to a simple probability distribution, e.g., Poisson. However, the distribution of the original data is changed dramatically by preprocessing operations. For such an algorithm, it is preferable to incorporate these estimates (i.e., normalization, attenuation, randoms, scatter) directly into the D-D model of the data acquisition process as described in Section V, (17)–(22) and in the references cited at (22), rather than doing preprocessing operations on the data.

In SPECT, a preprocessing operation can be applied to the data to subtract an estimate of the scatter contribution (and there is no random contribution in this case). In SPECT, no preprocessing operation can remove the effect of attenuation, but in practice some approximate techniques, such as averaging opposing views, can reduce its effect [131]. Approximate postprocessing techniques [198] have also been devised that reduce the effect of attenuation when applied to the reconstructed image. Although they do not have a strong theoretical justification, these preprocessing and postprocessing techniques can lead to surprisingly good results when applied in combination with the basic convolution-backprojection method, and this approach is widely used in practical applications of SPECT.

C. Fourier Deblurring of Data in SPECT, and Fourier Rebinning of Data in PET

We now return to considering reconstruction of the emission distribution in SPECT using methods derived from the C-C approach. In addition to the significant problem of attenuation in SPECT, there is a further problem concerning the model of the data collection process. The spatially invariant model involves integration with uniform weight along lines, but this is not a good approximation for SPECT. In SPECT, each element of the detector receives photons from a narrow cone of directions, defined by the physical aperture of a collimator device that rejects most of the incoming photons. The most common form of collimator consists of a thick slab of shielding material (e.g., lead) having a large number of small diameter parallel holes and placed adjacent to the front surface of the detector. Another form of collimator consists of a single pinhole aperture in a sheet of shielding material that is placed some distance from the front surface of the detector. In each case, the response of an element of the detector to a point source of photons varies significantly as a function of the distance from the point to the entry aperture of the collimator.

Preprocessing methods have been devised to reduce the effect of the distance-dependent response of the collimator on the data at the input of the reconstruction algorithm, so that methods derived from the line integral model can achieve better results when applied to SPECT data. We now describe one particular preprocessing method for the case of parallel-ray projections, such as those obtained using a parallel-hole collimator. We describe this method here, because the principle involved is also the basis of a popular preprocessing method in PET.

We consider nonoblique $(\theta = 0)$ projections for the 2-D slice $z = z' = 0$, so that these projections are $p_{\phi,0}(x', 0)$. We consider the Fourier decomposition of these projections, where the Fourier decomposition involves both variables x' and ϕ and is obtained by a Fourier transform with respect to

x', with continuous frequency variable $\omega_{x'}$, and by a Fourier series representation in ϕ, with integer harmonic index k_ϕ. We denote the Fourier coefficients by $\hat{\hat{p}}_{k_\phi,0}(\omega_{x'},0)$ with the Fourier pair defined by

$$\hat{\hat{p}}_{k_\phi,0}(\omega_{x'},0) = \frac{1}{2\pi}\int_0^{2\pi}\int_{-\infty}^{\infty} p_{\phi,0}(x',0)e^{-i(\omega_{x'}x'+k_\phi\phi)}\,dx'\,d\phi \tag{38}$$

$$p_{\phi,0}(x',0) = \frac{1}{2\pi}\int_{-\infty}^{\infty}\sum_{k=-\infty}^{\infty}\hat{\hat{p}}_{k_\phi,0}(\omega_{x'},0)e^{i(\omega_{x'}x'+k_\phi\phi)}\,d\omega_{x'}. \tag{39}$$

It is shown in [199]–[201] that this Fourier representation has a special property, known as the "frequency-distance relation" for the Fourier coefficients, that is valid asymptotically at large radial frequencies $\omega_{x'}$. This relation states that as ϕ goes from 0 to 2π, the most significant contribution of an arbitrary point object to the value of the coefficient $\hat{\hat{p}}_{k_\phi,0}(\omega_{x'},0)$ occurs at an angle ϕ such that the point's distance coordinate y' along the line of integration is $(-k_\phi/\omega_{x'})$. This relation implies that one can modify the band of coefficients in the Fourier domain that have almost the same value of $(-k_\phi/\omega_{x'})$ and obtain the effect of modifying contributions to the projection data that have originated within a small range of distances from the detector. In SPECT, it is therefore possible to separate approximately the distance-dependent spatial blurring factors in the Fourier coefficients of the blurred projection data, and perform distance-dependent spatial filtering of this data prior to reconstruction. This approach has been investigated and compared with other approaches in, e.g., [202]–[205].

It is shown in [206]–[208] that the frequency-distance relation also leads to a very useful preprocessing method for PET data, known as Fourier rebinning (FORE). In PET, the same Fourier decomposition with respect to the variables x' and ϕ is applied to the oblique (nonzero θ) projections $p_{\phi,\theta}(x',z')$ to obtain coefficients $\hat{\hat{p}}_{k_\phi,\theta}(\omega_{x'},z')$. It can be shown that the frequency-distance relation continues to hold in the transverse planes (z constant), so that the most significant contributions to the value of this coefficient come from emissions originating at a distance y' along the lines of integration for which the transverse component of y', relative to the center of the line, is $(-k_\phi/\omega_{x'})$. Since the slope of the lines is $(\tan\theta)$, the corresponding component in the z direction, again relative to the center of the line, is $(-k_\phi/\omega_{x'})\tan\theta$. This provides a link between the Fourier coefficients of the oblique projections and another set of Fourier coefficients associated with the nonoblique $(\theta=0)$ projections, so that

$$\hat{\hat{p}}_{k_\phi,\theta}(\omega_{x'},z') \approx \hat{\hat{p}}_{k_\phi,0}(\omega_{x'},\, z^* + (-k_\phi/\omega_{x'})\tan\theta) \tag{40}$$

where z^* is the z coordinate of the center of the lines for this (θ,z'). This approximate relation (whose accuracy improves as the radial frequency $\omega_{x'}$ increases) leads to a preprocessing method for PET that takes the oblique projections that are measured over the PET scanner's range of θ, and produces a set of equivalent projections for $\theta=0$. For each slice z, the projection data $p_{\phi,0}(x',z)$ can be reconstructed by a 2-D algorithm. This preprocessing method therefore decomposes the problem of 3-D reconstruction in PET into a set of 2-D problems, which greatly reduces the amount of computation required for reconstruction.

A similar decomposition can be done exactly by a rebinning method known as FOREX [207], [208], but this method requires estimation of the unmeasured parts of the projections, as needed for the 3-D direct Fourier method and also for the 3-D convolution-backprojection method (see Section VI-A and Fig. 6). A similar decomposition can be done exactly by another rebinning method known as FORE-J [209], which operates directly (without an estimation step) on the axially truncated data measured by the PET detector system, as is also the case with the approximate method FORE. The relationship between these three rebinning methods (FORE, FOREX, FORE-J) is discussed in [209].

After the PET data are rebinned by one of these methods into a set of independent projections of 2-D slices, the 2-D reconstructions can be done by an algorithm derived from the C-C model, such as convolution-backprojection. Alternatively, the 2-D reconstruction can be done by an algorithm derived from the D-D model. Since the rebinning operation is derived from the C-C model, the use of an algorithm derived from the D-D model leads to a hybrid approach to the overall reconstruction problem. Note that the rebinning operation, being derived from the C-C model, requires as its input the projection data resulting from corrections to the measured PET data for normalization, attenuation, scatter, and randoms, as described in the text associated with (37). The hybrid approach using a reconstruction algorithm derived from the D-D model has the advantage over the uniformly C-C approach of being able to take account of the statistical distribution of the noise in the rebinned data, if this is available, although it is difficult (and perhaps impossible) to fully characterize the probability distribution of the data that result from the preprocessing operations done by the Fourier rebinning methods. The difficulty arises not only from the nature of the rebinning operations themselves, which involve many different linear combinations of the Fourier coefficients of different projections, but also from the fact that these operations are being done on data that have already undergone corrections, which have modified the statistical distribution of the data from its original Poisson distribution. However, it is possible to obtain estimates of the variance by making some reasonable approximations, and estimates of the variance of the rebinned data are being used in recent hybrid methods [210]–[212].

VIII. Discussion—Linearity Versus Optimality

The C-C formulation of the reconstruction problem leads to inversion formulas and algorithms that involve only linear operations on the data. LSI algorithms such as convolution-backprojection are characterized by a point-spread function (PSF), which is the reconstructed image of a point emission source. For such an algorithm, the PSF does not depend on the location of the point within the field of view. In addition, the PSF does not depend on the emission activity level of the

local background on which the point source is superimposed, or on the emissions from other parts of the object. The central part of the PSF has the form of a narrow bell-shaped peak, whose full width at half maximum (FWHM) can be used to specify the spatial resolution of the reconstructed image, which is spatially invariant and object independent.

For linear algorithms, the propagation of noise from the data to the image can be analyzed using the standard results of linear systems theory (see, e.g., [3] and [213]). In emission tomography, the noise in the data is signal-dependent, and linear estimators are not statistically optimal. For Poisson data, the variance is equal to the mean, so that a high-count measurement has a low relative noise level (standard deviation/mean) but has a high absolute noise level (standard deviation). The backprojection of a high-count measurement introduces a high absolute level of noise along a line through the image, leading to a high relative noise in low-count regions, as discussed in [214] and [215]. For linear methods, most of the noise in the image is caused by high-count measurements spread across the image, so the noise level is quite uniform throughout the image.

Maximum likelihood estimators are nonlinear, and their noise characteristics are quite different. Such estimators are able to localize the absolute noise levels in the image, so that the local image variance remains proportional to the local count level, resulting in images where the noise is high in regions of high emission activity and the noise is low in regions of low emission activity, as clearly demonstrated in [215] and [216]. These images appear less noisy and more visually appealing than images reconstructed by linear methods. The analysis of the noise properties of nonlinear methods is of course much more difficult than for linear methods, although considerable progress has been made in recent years [213], [214], [216]–[220].

A significant problem with nonlinear methods is that the spatial resolution, as indicated by the PSF, is spatially variant and object dependent [221], [222]. This is a significant problem for applications that require absolute quantitation [223], [224], especially those involving determination of the parameters of a kinetic model from a time sequence of images [225]. In addition to the position and object dependence, the PSF may be highly asymmetric, indicating that the local smoothing is strongly anisotropic, as demonstrated in [226]. Such blurring distorts the shapes of objects so, for example, circular objects appear elliptical.

These effects result from the use of the conventional objective function for penalized log likelihood stated in (15) and (23), where the penalty term $\beta R(\tilde{f})$ has the same voxel weights throughout the image. In order to achieve uniform spatial resolution in the image, the regularization needs to be *spatially variant* to compensate for the variations in count density in the data and in the image [222]. Recent papers describe methods to design the spatially variant weights of the penalty function to achieve near-uniform resolution [220], [226] or to optimize the local contrast to noise ratio [219], [220] in order to improve lesion detectability, which has been confirmed by recent analysis [213] to be better than the detectability achievable by linear reconstruction methods. It is likely that these more sophisticated regularization methods will become increasingly important in the future as applications of PET and SPECT demand more quantitative information from the reconstructed images produced by maximum likelihood estimators.

IX. Conclusion

This paper has used the various models of the data collection process as the framework for presenting an overview of the wide variety of methods that have been developed for image reconstruction in PET and SPECT. The overall sequence of the major sections in the paper, and the presentation within each major section, both proceed from the more realistic and general models to those that are idealized and application-specific. For most of the topics, the description proceeds from the 3-D case to the 2-D case.

For the methods based on the more general models, there is no fundamental difference between 3-D and 2-D, or between PET and SPECT. For the methods based on inversion formulas derived from idealized models, the 3-D case is fundamentally different from the 2-D case, and the effect of photon attenuation is fundamentally different in SPECT, compared to the much simpler situation in PET.

Historically, the development of image reconstruction methods began with 2-D methods that were based on idealized models and that were developed for specific applications. The trend today is increasingly toward more versatile 3-D methods for static and dynamic (3-D, time) reconstruction that are based on more general and more realistic models, into which the application-specific physics and geometry of the data collection process are incorporated. However, such methods require large amounts of computation, and their use at the present time is often limited by the computational power that is available. Since the computational power available to typical users is increasing rapidly, these methods will play an increasingly important role in the future.

A wide variety of methods has been developed for image reconstruction in PET and SPECT, since these include a wide variety of applications having different acquisition geometries, different amounts of noise in the data, different sizes of the data sets and image grids, different computational resources or time constraints, and different end uses for the images (e.g., qualitative use of images for tumor detection tasks versus quantitative use for parameter estimation tasks). For these reasons, there can be no single universal algorithm for image reconstruction that is suitable for all of the various applications of PET and SPECT.

The paper has presented a broad overview of algorithms for PET and SPECT. It is hoped that the list of references will provide a useful starting point for the reader who is interested in more detailed descriptions of these algorithms and their applications.

Acknowledgment

The authors thank the Guest Editors for their encouragement and advice, and thank the reviewers for their detailed

comments. The authors are grateful for the many comments and suggestions received from their colleagues: Y. Censor, M. Defrise, T. Elfving, C. L. Epstein, J. A. Fessler, J. S. Karp, I. G. Kazantsev, L. M. Popescu, and S. Surti.

REFERENCES

[1] S. Webb, *From the Watching of Shadows*. Bristol, U.K.: Adam Hilger, 1990.

[2] J. A. Sorenson and M. E. Phelps, *Physics in Nuclear Medicine*. Philadelphia, PA: Saunders, 1987.

[3] H. H. Barrett and W. Swindell, *Radiological Imaging: The Theory of Image Formation, Detection, and Processing*. San Diego, CA: Academic, 1981.

[4] S. Webb, Ed., *The Physics of Medical Imaging*. Philadelphia, PA: Inst. of Physics, 1988.

[5] K. K. Shung, M. B. Smith, and B. M. W. Tsui, *Principles of Medical Imaging*. San Diego, CA: Academic, 1992.

[6] Z. H. Cho, J. P. Jones, and M. Singh, *Foundations of Medical Imaging*. New York: Wiley, 1993.

[7] A. Macovski, *Medical Imaging Systems*. Paramus, NJ: Prentice-Hall, 1997.

[8] A. C. Kak and M. Slaney, *Principles of Computerized Tomographic Imaging*. Philadelphia, PA: SIAM, 2001.

[9] W. A. Kalender, *Computed Tomography: Fundamentals, System Technology, Image Quality, Applications*. New York: Wiley, 2000.

[10] E. M. Haacke, R. W. Brown, M. R. Thompson, and R. Venkatesan, *Magnetic Resonance Imaging: Physical Principles and Sequence Design*. New York: Wiley, 1999.

[11] Z.-P. Liang and P. C. Lauterbur, *Principles of Magnetic Resonance Imaging: A Signal Processing Perspective*. New York: IEEE Press, 2000.

[12] R. J. English, *SPECT: Single-Photon Emission Computed Tomography: A Primer*. Reston, VA: Soc. of Nuclear Medicine, 1995.

[13] B. Bendriem and D. W. Townsend, Eds., *The Theory and Practice of 3D PET*. Dordrecht, The Netherlands: Kluwer, 1998.

[14] B. M. W. Tsui, X. D. Zhao, E. C. Frey, and W. H. McCartney, "Quantitative single-photon emission computed tomography: Basics and clinical considerations," *Seminars Nucl. Med.*, vol. 24, no. 1, pp. 38–65, 1994.

[15] M. S. Rosenthal, J. Cullom, W. Hawkins, S. C. Moore, B. M. W. Tsui, and M. Yester, "Quantitative SPECT imaging: A review and recommendations by the focus committee of the Society of Nuclear Medicine computer and instrumentation council," *J. Nucl. Med.*, vol. 36, no. 8, pp. 1489–1513, 1995.

[16] J. M. Links, "Advances in nuclear medicine instrumentation: Considerations in the design and selection of an imaging system," *Eur. J. Nucl. Med.*, vol. 25, no. 10, pp. 1453–1466, 1998.

[17] D. L. Bailey, J. S. Karp, and S. Surti, "Physics and instrumentation in positron emission tomography," in *Positron Emission Tomography: Basic Science and Clinical Practice*, P. E. Valk, D. L. Bailey, D. W. Townsend, and M. N. Maisey, Eds. Berlin, Germany: Springer-Verlag, 2003.

[18] H. H. Barrett and K. J. Myers, Foundations of Image Science. New York: Wiley, 2003, to be published.

[19] H. H. Barrett, J. N. Aarsvold, and T. J. Roney, "Null functions and eigenfunctions: Tools for the analysis of imaging systems," in *Information Processing in Medical Imaging*, D. A. Ortendahl and J. Llacer, Eds. New York: Wiley-Liss, 1991, pp. 211–226.

[20] R. Van de Walle, H. H. Barrett, K. J. Myers, M. I. Altbach, B. Desplanques, A. F. Gmitro, J. Cornelis, and I. Lemahieu, "Reconstruction of MR images from data acquired on a general nonregular grid by pseudoinverse calculation," *IEEE Trans. Med. Imag.*, vol. 19, pp. 1160–1167, Dec. 2000.

[21] M. Bertero and P. Boccacci, *Introduction to Inverse Problems in Imaging*. Bristol, U.K.: Inst. of Physics, 1998.

[22] J. M. Ollinger and J. A. Fessler, "Positron-emission tomography," *IEEE Signal Processing Mag.*, vol. 14, pp. 43–55, Jan. 1997.

[23] R. M. Leahy and J. Qi, "Statistical approaches in quantitative positron emission tomography," *Stat. Comput.*, vol. 10, no. 2, pp. 147–165, 2000.

[24] L. Bouwens, R. Van de Walle, J. Nuyts, M. Koole, Y. D'Asseler, S. Vandenberghe, I. Lemahieu, and R. A. Dierckx, "Image-correction techniques in SPECT," *Comput. Med. Imaging Graph.*, vol. 25, no. 2, pp. 117–126, 2001.

[25] F. J. Beekman, C. Kamphuis, M. A. King, P. P. van Rijk, and M. A. Viergever, "Improvement of image resolution and quantitative accuracy in clinical single photon emission computed tomography," *Comput. Med. Imaging Graph.*, vol. 25, no. 2, pp. 135–146, 2001.

[26] J. A. Fessler. (2001) Statistical image reconstruction. [Online]. Available: http://www.eecs.umich.edu/~fessler/

[27] D. L. Snyder and M. I. Miller, *Random Point Processes in Time and Space*. New York: Springer-Verlag, 1991.

[28] S. N. Evans and P. B. Stark, "Inverse problems as statistics," *Inverse Problems*, vol. 18, no. 4, pp. R55–R97, 2002.

[29] D. F. Yu and J. A. Fessler, "Mean and variance of single photon counting with deadtime," *Phys. Med. Biol.*, vol. 45, no. 7, pp. 2043–2056, 2000.

[30] ——, "Mean and variance of coincidence counting with deadtime," *Nucl. Instrum. Methods Phys. Res. A*, vol. 488, no. 1-2, pp. 362–374, 2002.

[31] J. M. Wagner, F. Noo, R. Clackdoyle, G. Bal, and P. Christian, "Attenuation correction for rotating slant-hole (RSH) SPECT using exact rebinning," *IEEE Trans. Nucl. Sci.*, vol. 50, pp. 110–116, Feb. 2003.

[32] W. H. Baird, E. C. Frey, B. M. W. Tsui, Y. Wang, and D. E. Wessell, "Evaluation of rotating slant-hole SPECT mammography using Monte Carlo simulation methods," *IEEE Trans. Nucl. Sci.*, vol. 50, pp. 105–109, Feb. 2003.

[33] G. L. Zeng, D. Gagnon, C. G. Matthews, J. A. Kolthammer, J. D. Radachy, and W. G. Hawkins, "Image reconstruction algorithm for a rotating slat collimator," *Med. Phys.*, vol. 29, no. 7, pp. 1406–1412, 2002.

[34] S. D. Metzler, J. E. Bowsher, K. L. Greer, and R. J. Jaszczak, "Analytic determination of the pinhole collimator's point-spread function and RMS resolution with penetration," *IEEE Trans. Med. Imag.*, vol. 21, pp. 878–887, Aug. 2002.

[35] M. C. Wu, B. H. Hasegawa, and M. W. Dae, "Performance evaluation of a pinhole SPECT system for myocardial perfusion imaging of mice," *Med. Phys.*, vol. 29, no. 12, pp. 2830–2839, 2002.

[36] R. J. Jaszczak, J. Y. Li, H. Wang, M. R. Zalutsky, and R. E. Coleman, "Pinhole collimation for ultra-high-resolution, small-field-of-view SPECT," *Phys. Med. Biol.*, vol. 39, no. 3, pp. 425–437, 1994.

[37] J. Y. Li, R. J. Jaszczak, and R. E. Coleman, "A filtered backprojection algorithm for axial head motion correction in fan-beam SPECT," *Phys. Med. Biol.*, vol. 40, no. 12, pp. 2053–2063, 1995.

[38] J. Y. Li, R. J. Jaszczak, K. L. Greer, and R. E. Coleman, "Implementation of an accelerated iterative algorithm for cone-beam SPECT," *Phys. Med. Biol.*, vol. 39, no. 3, pp. 643–653, 1994.

[39] G. L. Zeng, Y. Weng, and G. T. Gullberg, "Iterative reconstruction with attenuation compensation from cone-beam projections acquired via nonplanar orbits," *IEEE Trans. Nucl. Sci.*, vol. 44, pp. 98–106, Feb. 1997.

[40] C. D. Stone, M. F. Smith, K. L. Greer, and R. J. Jaszczak, "A combined half-cone beam and parallel hole collimation system for SPECT brain imaging," *IEEE Trans. Nucl. Sci.*, vol. 45, pp. 1219–1224, June 1998.

[41] G. L. Zeng and G. T. Gullberg, "Iterative and analytical reconstruction algorithms for varying-focal-length cone-beam projections," *Phys. Med. Biol.*, vol. 43, no. 4, pp. 811–821, 1998.

[42] J. S. You, Z. R. Liang, and G. L. Zeng, "A unified reconstruction framework for both parallel-beam and variable focal-length fan-beam collimators by a Cormack-type inversion of exponential Radon transform," *IEEE Trans. Med. Imag.*, vol. 18, pp. 59–65, Jan. 1999.

[43] T. K. Lewellen, "Time-of-flight PET," *Seminars Nucl. Med.*, vol. 28, no. 3, pp. 268–275, 1998.

[44] F. Natterer, *The Mathematics of Computerized Tomography*. Chichester, U.K.: Wiley, 1986.

[45] F. Natterer and F. Wübbeling, *Mathematical Methods in Image Reconstruction*. Philadelphia, PA: SIAM, 2001.

[46] R. L. Parker, *Geophysical Inverse Theory*. Princeton, NJ: Princeton Univ. Press, 1994.

[47] G. Minerbo, "MENT: A maximum entropy algorithm for reconstructing a source from projection data," *Comput. Graph. Image Process.*, vol. 10, no. 1, pp. 48–68, 1979.

[48] T. S. Durrani and C. E. Goutis, "Optimisation techniques for digital image reconstruction from their projections," *Proc. IEE—Comput. Digital Tech.*, pt. E, vol. 127, no. 5, pp. 161–169, 1980.

[49] F. Natterer, "Efficient implementation of optimal algorithms in computerized tomography," *Math. Methods Appl. Sci.*, vol. 2, pp. 545–555, 1980.

[50] M. H. Buonocore, W. R. Brody, and A. Macovski, "A natural pixel decomposition for two-dimensional image reconstruction," *IEEE Trans. Biomed. Eng.*, vol. BME–28, pp. 69–78, Feb. 1981.

[51] G. T. Gullberg, Y. L. Hsieh, and G. L. Zeng, "An SVD reconstruction algorithm using a natural pixel representation of the attenuated Radon transform," *IEEE Trans. Nucl. Sci.*, vol. 43, pp. 295–303, Feb. 1996.
[52] Y. L. Hsieh, G. T. Gullberg, G. L. Zeng, and R. H. Huesman, "Image reconstruction using a generalized natural pixel basis," *IEEE Trans. Nucl. Sci.*, vol. 43, pp. 2306–2319, Aug. 1996.
[53] Y. L. Hsieh, G. L. Zeng, and G. T. Gullberg, "Projection space image reconstruction using strip functions to calculate pixels more natural for modeling the geometric response of the SPECT collimator," *IEEE Trans. Med. Imag.*, vol. 17, pp. 24–44, Feb. 1998.
[54] M. Mimura, T. Obi, M. Yamaguchi, and N. Ohyama, "Correction of nonuniform response in the reconstruction for single photon emission computed tomography with a spatially varying focal length collimator," *Opt. Rev.*, vol. 5, no. 5, pp. 275–279, 1998.
[55] J. R. Baker, T. F. Budinger, and R. H. Huesman, "Generalized approach to inverse problems in tomography: Image reconstruction for spatially variant systems using natural pixels," *Crit. Rev. Biomed. Eng.*, vol. 20, no. 1–2, pp. 47–71, 1992.
[56] T. Yamaya, T. Obi, M. Yamaguchi, and N. Ohyama, "High-resolution image reconstruction method for time-of-flight positron emission tomography," *Phys. Med. Biol.*, vol. 45, no. 11, pp. 3125–3134, 2000.
[57] G. T. Gullberg, "Entropy and transverse section reconstruction," in *Information Processing in Scintigraphy: Proceedings of the IVth International Conference*, C. Raynaud and A. Todd-Pokropek, Eds. Orsay, France: Commissariat à l'Énergie Atomique, 1975, pp. 325–332.
[58] B. F. Logan and L. A. Shepp, "Optimal reconstruction of a function from its projections," *Duke Math. J.*, vol. 42, pp. 645–659, 1975.
[59] I. G. Kazantsev, R. Van de Walle, and I. Lemahieu, "Ridge functions, natural pixels and minimal norm reconstruction," *IEEE Trans. Nucl. Sci.*, vol. 47, pp. 1118–1122, June 2000.
[60] D. C. Solmon, "The X-ray transform," *J. Math. Anal. Appl.*, vol. 56, pp. 61–83, 1976.
[61] C. Hamaker and D. C. Solmon, "The angles between the null spaces of X-rays," *J. Math. Anal. Appl.*, vol. 62, pp. 1–23, 1978.
[62] G. T. Herman and A. Lent, "Iterative reconstruction algorithms," *Comput. Biol. Med.*, vol. 6, pp. 273–294, 1976.
[63] J. A. Fessler, "Penalized weighted least-squares image reconstruction for positron emission tomography," *IEEE Trans. Med. Imag.*, vol. 13, pp. 290–300, June 1994.
[64] A. P. Dempster, N. M. Laird, and D. B. Rubin, "Maximum likelihood from incomplete data via the EM algorithm," *J. R. Stat. Soc. B—Methodolog.*, vol. 39, no. 1, pp. 1–38, 1977.
[65] G. J. McLachlan and T. Krishnan, *The EM Algorithm and Extensions*. New York: Wiley, 1997.
[66] P. P. B. Eggermont and V. N. LaRiccia, *Maximum Penalized Likelihood Estimation, Volume I: Density Estimation*. New York: Springer-Verlag, 2001.
[67] L. A. Shepp and Y. Vardi, "Maximum likelihood reconstruction for emission tomography," *IEEE Trans. Med. Imag.*, vol. 1, pp. 113–122, Oct. 1982.
[68] K. Lange and R. Carson, "EM reconstruction algorithms for emission and transmission tomography," *J. Comput. Assist. Tomography*, vol. 8, no. 2, pp. 306–316, 1984.
[69] Y. Vardi, L. A. Shepp, and L. Kaufman, "A statistical model for positron emission tomography," *J. Amer. Stat. Assoc.*, vol. 80, no. 389, pp. 8–20, 1985.
[70] H. M. Hudson and R. S. Larkin, "Accelerated image reconstruction using ordered subsets of projection data," *IEEE Trans. Med. Imag.*, vol. 13, pp. 601–609, Dec. 1994.
[71] C. L. Byrne, "Accelerating the EMML algorithm and related iterative algorithms by rescaled block-iterative methods," *IEEE Trans. Image Processing*, vol. 7, pp. 100–109, Jan. 1998.
[72] J. A. Browne and A. R. De Pierro, "A row-action alternative to the EM algorithm for maximizing likelihoods in emission tomography," *IEEE Trans. Med. Imag.*, vol. 15, pp. 687–699, Oct. 1996.
[73] S. Matej and J. A. Browne, "Performance of a fast maximum likelihood algorithm for fully 3D PET reconstruction," in *Three-Dimensional Image Reconstruction in Radiology and Nuclear Medicine*, P. Grangeat and J.-L. Amans, Eds. Dordrecht, The Netherlands: Kluwer, 1996, pp. 297–316.
[74] M. E. Daube-Witherspoon, S. Matej, J. S. Karp, and R. M. Lewitt, "Application of the row action maximum likelihood algorithm with spherical basis functions to clinical PET imaging," *IEEE Trans. Nucl. Sci.*, vol. 48, pp. 24–30, Feb. 2001.
[75] M. Yavuz and J. A. Fessler, "New statistical models for randoms-precorrected PET scans," in *Information Processing in Medical Imaging*, J. Duncan and G. Gindi, Eds. Berlin, Germany: Springer-Verlag, 1997, pp. 190–203.
[76] ——, "Statistical image reconstruction methods for randoms-precorrected PET scans," *Med. Image Anal.*, vol. 2, no. 4, pp. 369–378, 1998.
[77] ——, "Penalized-likelihood estimators and noise analysis for randoms-precorrected PET transmission scans," *IEEE Trans. Med. Imag.*, vol. 18, pp. 665–674, Aug. 1999.
[78] J. Qi, R. M. Leahy, C. Hsu, T. H. Farquhar, and S. R. Cherry, "Fully 3D Bayesian image reconstruction for the ECAT EXACT HR+," *IEEE Trans. Nucl. Sci.*, vol. 45, pp. 1096–1103, June 1998.
[79] R. M. Lewitt, "Multidimensional digital image representations using generalized Kaiser-Bessel window functions," *J. Opt. Soc. Amer. A*, vol. 7, no. 10, pp. 1834–1846, 1990.
[80] ——, "Alternatives to voxels for image representation in iterative reconstruction algorithms," *Phys. Med. Biol.*, vol. 37, no. 3, pp. 705–716, 1992.
[81] S. Matej and R. M. Lewitt, "Practical considerations for 3D image reconstruction using spherically-symmetric volume elements," *IEEE Trans. Med. Imag.*, vol. 15, pp. 68–78, Feb. 1996.
[82] ——, "Efficient 3D grids for image reconstruction using spherically-symmetric volume elements," *IEEE Trans. Nucl. Sci.*, vol. 42, pp. 1361–1370, Aug. 1995.
[83] J. Qi, R. M. Leahy, S. R. Cherry, A. Chatziioannou, and T. H. Farquhar, "High-resolution 3D Bayesian image reconstruction using the microPET small-animal scanner," *Phys. Med. Biol.*, vol. 43, pp. 1001–1013, 1998.
[84] D. W. Shattuck, J. Rapela, E. Asma, A. Chatziioannou, J. Qi, and R. M. Leahy, "Internet2-based 3D PET image reconstruction using a PC cluster," *Phys. Med. Biol.*, vol. 47, no. 15, pp. 2785–2795, 2002.
[85] I. Laurette, G. L. Zeng, A. Welch, P. E. Christian, and G. T. Gullberg, "A three-dimensional ray-driven attenuation, scatter and geometric response correction technique for SPECT in inhomogeneous media," *Phys. Med. Biol.*, vol. 45, no. 11, pp. 3459–3480, 2000.
[86] J. Hamill and T. Bruckbauer, "Iterative reconstruction methods for high-throughput PET tomographs," *Phys. Med. Biol.*, vol. 47, no. 15, pp. 2627–2636, 2002.
[87] J. Nuyts, C. Michel, and P. Dupont, "Maximum-likelihood expectation-maximization reconstruction of sinograms with arbitrary noise distribution using NEC-transformations," *IEEE Trans. Med. Imag.*, vol. 20, pp. 365–375, May 2001.
[88] J. Nuyts, D. Bequé, P. Dupont, and L. Mortelmans, "A concave prior penalizing relative differences for maximum-a-posteriori reconstruction in emission tomography," *IEEE Trans. Nucl. Sci.*, vol. 49, pp. 56–60, Feb. 2002.
[89] D. F. Yu and J. A. Fessler, "Edge-preserving tomographic reconstruction with nonlocal regularization," *IEEE Trans. Med. Imag.*, vol. 21, pp. 159–173, Feb. 2002.
[90] A. S. Willsky, "Multiresolution Markov models for signal and image processing," *Proc. IEEE*, vol. 90, pp. 1396–1458, Aug. 2002.
[91] J. E. Bowsher, V. E. Johnson, T. G. Turkington, R. J. Jaszczak, C. E. Floyd, and R. E. Coleman, "Bayesian reconstruction and use of anatomical a priori information for emission tomography," *IEEE Trans. Med. Imag.*, vol. 15, pp. 673–686, Oct. 1996.
[92] S. Alenius and U. Ruotsalainen, "Generalization of median root prior reconstruction," *IEEE Trans. Med. Imag.*, vol. 21, pp. 1413–1420, Nov. 2002.
[93] E. U. Mumcuoglu, R. Leahy, S. R. Cherry, and Z. Y. Zhou, "Fast gradient-based methods for Bayesian reconstruction of transmission and emission PET images," *IEEE Trans. Med. Imag.*, vol. 13, pp. 687–701, Dec. 1994.
[94] E. U. Mumcuoglu, R. M. Leahy, and S. R. Cherry, "Bayesian reconstruction of PET images: Methodology and performance analysis," *Phys. Med. Biol.*, vol. 41, no. 9, pp. 1777–1807, 1996.
[95] G. Chinn and S. C. Huang, "A general class of preconditioners for statistical iterative reconstruction of emission computed tomography," *IEEE Trans. Med. Imag.*, vol. 16, pp. 1–10, Feb. 1997.
[96] A. Chatziioannou, J. Qi, A. Moore, A. Annala, K. Nguyen, R. Leahy, and S. R. Cherry, "Comparison of 3-D maximum a posteriori and filtered backprojection algorithms for high-resolution animal imaging with microPET," *IEEE Trans. Med. Imag.*, vol. 19, pp. 507–512, May 2000.
[97] L. Bouwens, R. Van de Walle, H. Gifford, M. King, I. Lemahieu, and R. A. Dierckx, "LMIRA: List-mode iterative reconstruction algorithm for SPECT," *IEEE Trans. Nucl. Sci.*, vol. 48, pp. 1364–1370, Aug. 2001.
[98] L. R. Bouwens, H. Gifford, R. Van de Walle, M. A. King, I. Lemahieu, and R. A. Dierckx, "Resolution recovery for list-mode reconstruction in SPECT," *Phys. Med. Biol.*, vol. 46, no. 8, pp. 2239–2253, 2001.

[99] S. J. Wilderman, J. A. Fessler, N. H. Clinthorne, J. W. LeBlanc, and W. L. Rogers, "Improved modeling of system response in list mode EM reconstruction of Compton scatter camera images," *IEEE Trans. Nucl. Sci.*, vol. 48, pp. 111–116, Feb. 2001.

[100] D. L. Snyder, L. J. Thomas Jr., and M. M. Ter-Pogossian, "A mathematical model for positron emission tomography systems having time-of-flight measurements," *IEEE Trans. Nucl. Sci.*, vol. 28, pp. 3575–3583, June 1981.

[101] D. L. Snyder and D. G. Politte, "Image reconstruction from list-mode data in an emission tomography system having time-of-flight measurements," *IEEE Trans. Nucl. Sci.*, vol. 30, pp. 1843–1849, June 1983.

[102] H. H. Barrett, T. White, and L. C. Parra, "List-mode likelihood," *J. Opt. Soc. Amer. A*, vol. 14, no. 11, pp. 2914–2923, 1997.

[103] L. Parra and H. H. Barrett, "List-mode likelihood: EM algorithm and image quality estimation demonstrated on 2-D PET," *IEEE Trans. Med. Imag.*, vol. 17, pp. 228–235, Apr. 1998.

[104] C. Byrne, "Likelihood maximization for list-mode emission tomographic image reconstruction," *IEEE Trans. Med. Imag.*, vol. 20, pp. 1084–1092, Oct. 2001.

[105] R. H. Huesman, G. J. Klein, W. W. Moses, J. Qi, B. W. Reutter, and P. R. G. Virador, "List-mode maximum-likelihood reconstruction applied to positron emission mammography (PEM) with irregular sampling," *IEEE Trans. Med. Imag.*, vol. 19, pp. 532–537, May 2000.

[106] J. Qi, G. J. Klein, and R. H. Huesman, "Image properties of list-mode likelihood reconstruction for a rectangular positron emission mammograph with DOI measurements," *IEEE Trans. Nucl. Sci.*, vol. 48, pp. 1343–1349, Aug. 2001.

[107] J. Qi and R. H. Huesman, "Scatter correction for positron emission mammography," *Phys. Med. Biol.*, vol. 47, no. 15, pp. 2759–2771, 2002.

[108] A. J. Reader, K. Erlandsson, M. A. Flower, and R. J. Ott, "Fast accurate iterative reconstruction for low-statistics positron volume imaging," *Phys. Med. Biol.*, vol. 43, no. 4, pp. 835–846, 1998.

[109] ——, "Fast accurate iterative three-dimensional Bayesian reconstruction for low-statistics positron volume imaging," *IEEE Trans. Nucl. Sci.*, vol. 45, pp. 1090–1095, June 1998.

[110] A. J. Reader, K. Erlandsson, R. J. Ott, and M. A. Flower, "Attenuation and scatter correction of list-mode data driven iterative and analytic image reconstruction algorithms for rotating 3D PET systems," *IEEE Trans. Nucl. Sci.*, vol. 46, pp. 2218–2226, Dec. 1999.

[111] A. J. Reader, R. Manavaki, S. Zhao, P. J. Julyan, D. L. Hastings, and J. Zweit, "Accelerated list-mode EM algorithm," *IEEE Trans. Nucl. Sci.*, vol. 49, pp. 42–49, Feb. 2002.

[112] A. J. Reader, S. Ally, F. Bakatselos, R. Manavaki, R. J. Walledge, A. P. Jeavons, P. J. Julyan, S. Zhao, D. L. Hastings, and J. Zweit, "One-pass list-mode EM algorithm for high-resolution 3-D PET image reconstruction into large arrays," *IEEE Trans. Nucl. Sci.*, vol. 49, pp. 693–699, June 2002.

[113] R. Levkovitz, D. Falikman, M. Zibulevsky, A. Ben-Tal, and A. Nemirovski, "The design and implementation of COSEM, An iterative algorithm for fully 3-D listmode data," *IEEE Trans. Med. Imag.*, vol. 20, pp. 633–642, July 2001.

[114] M. Bocher, A. Balan, Y. Krausz, Y. Shrem, A. Lonn, M. Wilk, and R. Chisin, "Gamma camera-mounted anatomical X-ray tomography: Technology, system characteristics and first images," *European J. Nucl. Med.*, vol. 27, no. 6, pp. 619–627, 2000.

[115] J. A. Patton, D. Delbeke, and M. P. Sandler, "Image fusion using an integrated, dual-head coincidence camera with X-ray tube-based attenuation maps," *J. Nucl. Med.*, vol. 41, no. 8, pp. 1364–1368, 2000.

[116] A. J. Reader, "Penalised least squares image reconstruction from backprojection space for 3D PET," *IEEE Trans. Nucl. Sci.*, vol. 47, pp. 1072–1079, June 2000.

[117] A. J. Reader, S. Zhao, P. J. Julyan, D. L. Hastings, and J. Zweit, "Adaptive correction of scatter and random events for 3-D backprojected PET data," *IEEE Trans. Nucl. Sci.*, vol. 48, pp. 1350–1356, Aug. 2001.

[118] T. E. Nichols, J. Qi, and R. M. Leahy, "Continuous time dynamic PET imaging using list mode data," in *Information Processing in Medical Imaging*, A. Kuba, M. Šámal, and A. Todd-Pokropek, Eds. Berlin, Germany: Springer-Verlag, 1999, pp. 98–111.

[119] T. E. Nichols, J. Q. E. Asma, and R. M. Leahy, "Spatiotemporal reconstruction of list-mode PET data," *IEEE Trans. Med. Imag.*, vol. 21, pp. 396–404, Apr. 2002.

[120] Y. Censor, "Finite series-expansion reconstruction methods," *Proc. IEEE*, vol. 71, pp. 409–419, Mar. 1983.

[121] Y. Censor and S. A. Zenios, *Parallel Optimization: Theory, Algorithms, and Applications*. New York: Oxford Univ. Press, 1997.

[122] S. Vandenberghe, Y. D'Asseler, R. Van de Walle, T. Kauppinen, M. Koole, L. Bouwens, K. Van Laere, I. Lemahieu, and R. A. Dierckx, "Iterative reconstruction algorithms in nuclear medicine," *Comput. Med. Imaging Graph.*, vol. 25, no. 2, pp. 105–111, 2001.

[123] R. Leahy and C. Byrne, "Recent developments in iterative image reconstruction for PET and SPECT," *IEEE Trans. Med. Imag.*, vol. 19, pp. 257–260, Apr. 2000.

[124] M. F. Smith, "Generalized matrix inverse reconstruction for SPECT using a weighted singular value spectrum," *IEEE Trans. Nucl. Sci.*, vol. 43, pp. 2008–2017, June 1996.

[125] V. V. Selivanov and R. Lecomte, "Fast PET image reconstruction based on SVD decomposition of the system matrix," *IEEE Trans. Nucl. Sci.*, vol. 48, pp. 761–767, June 2001.

[126] S. Vollmar, C. Michel, J. T. Treffert, D. F. Newport, M. Casey, C. Knöss, K. Wienhard, X. Liu, M. Defrise, and W.-D. Heiss, "Heinzel-Cluster: Accelerated reconstruction for FORE and OSEM3D," *Phys. Med. Biol.*, vol. 47, no. 15, pp. 2651–2658, 2002.

[127] J. A. Fessler, "Statistical image reconstruction methods for transmission tomography," in *Handbook of Medical Imaging: Vol. 2, Medical Image Processing and Analysis*, M. Sonka and J. M. Fitzpatrick, Eds. Bellingham, WA: SPIE, 2000, pp. 1–70.

[128] R. Gordon, "A tutorial on ART (Algebraic Reconstruction Techniques)," *IEEE Trans. Nucl. Sci.*, vol. 21, pp. 78–93, June 1974.

[129] R. Gordon and G. T. Herman, "Three-dimensional reconstruction from projections: A review of algorithms," in *International Review of Cytology*, G. H. Bourne and J. F. Danielli, Eds. New York: Academic, 1974, vol. 38, pp. 111–151.

[130] T. F. Budinger and G. T. Gullberg, "Three-dimensional reconstruction in nuclear medicine emission imaging," *IEEE Trans. Nucl. Sci.*, vol. 21, pp. 2–20, June 1974.

[131] T. F. Budinger, G. T. Gullberg, and R. H. Huesman, "Emission computed tomography," in *Image Reconstruction from Projections: Implementation and Applications*, G. T. Herman, Ed. New York: Springer-Verlag, 1979, pp. 147–246.

[132] G. T. Herman, *Image Reconstruction from Projections: The Fundamentals of Computerized Tomography*. New York: Academic, 1980.

[133] ——, "Algebraic reconstruction techniques in medical imaging," in *Medical Imaging Systems Techniques and Applications: Computational Techniques*, C. T. Leondes, Ed. Amsterdam, The Netherlands: Gordon and Breach/OPA, 1998, pp. 1–42.

[134] H. H. Bauschke and J. M. Borwein, "On projection algorithms for solving convex feasibility problems," *SIAM Rev.*, vol. 38, no. 3, pp. 367–426, 1996.

[135] I. Csiszár and G. Tusnády, "Information geometry and alternating minimization procedures," *Stat. Decisions, Suppl. 1*, pp. 205–237, 1984.

[136] C. Byrne and Y. Censor, "Proximity function minimization using multiple Bregman projections, with applications to split feasibility and Kullback-Leibler distance minimization," *Ann. Oper. Res.*, vol. 105, pp. 77–98, 2001.

[137] Y. Censor, D. Gordon, and R. Gordon, "BICAV: A block-iterative parallel algorithm for sparse systems with pixel-related weighting," *IEEE Trans. Med. Imag.*, vol. 20, pp. 1050–1060, Oct. 2001.

[138] Y. Censor and T. Elfving, "Block-iterative algorithms with diagonally scaled oblique projections for the linear feasibility problem," *SIAM J. Matrix Anal. Appl.*, vol. 24, no. 1, pp. 40–58, 2002.

[139] Y. Censor, T. Elfving, and G. T. Herman, "Averaging strings of sequential iterations for convex feasibility problems," in *Inherently Parallel Algorithms in Feasibility and Optimization and Their Applications*, D. Butnariu, Y. Censor, and S. Reich, Eds. Amsterdam, The Netherlands: Elsevier, 2001, pp. 101–114.

[140] R. N. Bracewell, "Strip integration in radio astronomy," *Aust. J. Phys.*, vol. 9, pp. 198–217, 1956.

[141] ——, *The Fourier Transform and its Applications*. New York: McGraw-Hill, 1965.

[142] ——, *Two-Dimensional Imaging*. Englewood Cliffs, N.J.: Prentice-Hall, 1995.

[143] P. E. Kinahan and J. G. Rogers, "Analytic 3D image reconstruction using all detected events," *IEEE Trans. Nucl. Sci.*, vol. 36, pp. 964–968, Feb. 1989.

[144] M. Defrise and P. E. Kinahan, "Data acquisition and image reconstruction for 3D PET," in *The Theory and Practice of 3D PET*, B. Bendriem and D. W. Townsend, Eds. Dordrecht, The Netherlands: Kluwer, 1998, pp. 11–53.

[145] R. M. Lewitt, "Reconstruction algorithms: Transform methods," *Proc. IEEE*, vol. 71, pp. 390–408, Mar. 1983.

[146] R. N. Bracewell and A. C. Riddle, "Inversion of fan beam scans in radio astronomy," *Astrophys. J.*, vol. 150, no. 2P1, pp. 427–434, 1967.
[147] R. N. Bracewell, "Image reconstruction in radio astronomy," in *Image Reconstruction from Projections: Implementation and Applications*, G. T. Herman, Ed. New York: Springer-Verlag, 1979, pp. 81–104.
[148] D. J. DeRosier and A. Klug, "Reconstruction of 3-dimensional structures from electron micrographs," *Nature*, vol. 217, no. 5124, pp. 130–134, 1968.
[149] J. Frank, Ed., *Electron Tomography: Three-Dimensional Imaging with the Transmission Electron Microscope*. New York: Plenum, 1992.
[150] J. Frank, *Three-Dimensional Electron Microscopy of Macromolecular Assemblies*. San Diego: Academic, 1996.
[151] W. N. Brouw, "Aperture synthesis," in *Methods in Computational Physics*, B. Alder, S. Fernbach, and M. Rotenberg, Eds. New York: Academic, 1975, vol. 14, pp. 131–175.
[152] J. D. O'Sullivan, "A fast sinc function gridding algorithm for Fourier inversion in computer tomography," *IEEE Trans. Med. Imag.*, vol. 4, pp. 200–207, Dec. 1985.
[153] S. Matej and R. M. Lewitt, "3D-FRP: Direct Fourier reconstruction with Fourier reprojection for fully 3D PET," *IEEE Trans. Nucl. Sci.*, vol. 48, pp. 1378–1385, Aug. 2001.
[154] H. Schomberg and J. Timmer, "The gridding method for image reconstruction by Fourier transformation," *IEEE Trans. Med. Imag.*, vol. 14, pp. 596–607, Sept. 1995.
[155] V. Rasche, R. Proksa, R. Sinkus, P. Börnert, and H. Eggers, "Resampling of data between arbitrary grids using convolution interpolation," *IEEE Trans. Med. Imag.*, vol. 18, pp. 385–392, May 1999.
[156] H. Sedarat and D. G. Nishimura, "On the optimality of the gridding reconstruction algorithm," *IEEE Trans. Med. Imag.*, vol. 19, pp. 306–317, Apr. 2000.
[157] G. N. Ramachandran and V. A. Lakshminarayanan, "Three-dimensional reconstruction from radiographs and electron micrographs: Applications of convolutions instead of Fourier transforms," *Proc. Nat. Acad. Sci. USA*, vol. 68, no. 9, pp. 2236–2240, 1971.
[158] L. A. Shepp and B. F. Logan, "The Fourier reconstruction of a head section," *IEEE Trans. Nucl. Sci.*, vol. 21, pp. 21–43, June 1974.
[159] R. M. Lewitt, R. H. T. Bates, and T. M. Peters, "Image reconstruction from projections: II: Modified back-projection methods," *Optik*, vol. 50, pp. 85–109, 1978.
[160] S. W. Rowland, "Computer implementation of image reconstruction formulas," in *Image Reconstruction from Projections: Implementation and Applications*, G. T. Herman, Ed. New York: Springer-Verlag, 1979, pp. 9–79.
[161] M. Radermacher, "Weighted back-projection methods," in *Electron Tomography: Three-Dimensional Imaging with the Transmission Electron Microscope*, J. Frank, Ed. New York: Plenum, 1992, pp. 91–115.
[162] S. Bellini, M. Piacentini, C. Cafforio, and F. Rocca, "Compensation of tissue absorption in emission tomography," *IEEE Trans. Acoust., Speech, Signal Processing*, vol. 27, pp. 213–218, June 1979.
[163] O. Tretiak and C. Metz, "The exponential Radon transform," *SIAM J. Appl. Math.*, vol. 39, no. 2, pp. 341–354, 1980.
[164] C. E. Metz and X. C. Pan, "A unified analysis of exact methods of inverting the 2-D exponential Radon transform, with implications for noise control in SPECT," *IEEE Trans. Med. Imag.*, vol. 14, pp. 643–658, Dec. 1995.
[165] X. C. Pan and C. E. Metz, "Analysis of noise properties of a class of exact methods of inverting the 2-D exponential Radon transform," *IEEE Trans. Med. Imag.*, vol. 14, pp. 659–668, Dec. 1995.
[166] R. G. Novikov, "An inversion formula for the attenuated X-ray transformation," *C. R. Acad. Sci. Paris*, ser. I-Math., vol. 332, no. 12, pp. 1059–1063, 2001.
[167] F. Natterer, "Inversion of the attenuated Radon transform," *Inverse Problems*, vol. 17, no. 1, pp. 113–119, 2001.
[168] R. G. Novikov, "On the range characterization for the two-dimensional attenuated X-ray transformation," *Inverse Problems*, vol. 18, no. 3, pp. 677–700, 2002.
[169] L. A. Kunyansky, "A new SPECT reconstruction algorithm based on the Novikov explicit inversion formula," *Inverse Problems*, vol. 17, no. 2, pp. 293–306, 2001.
[170] J.-P. Guillement, F. Jauberteau, L. Kunyansky, R. Novikov, and R. Trebossen, "On single-photon emission computed tomography imaging based on an exact formula for the nonuniform attenuation correction," *Inverse Problems*, vol. 18, no. 6, pp. L11–L19, 2002.
[171] S. R. Deans, *The Radon Transform and Some of its Applications*. New York: Wiley, 1983.
[172] J. Radon, "On the determination of functions from their integral values along certain manifolds," *IEEE Trans. Med. Imag.*, vol. 5, pp. 170–176, Dec. 1986. Translated by P.C. Parks from the original German text.
[173] H. Hornich, "A tribute to Johann Radon," *IEEE Trans. Med. Imag.*, vol. 5, pp. 169–169, Dec. 1986. Translated by P.C. Parks from the original German text.
[174] F. Natterer and E. L. Ritman, "Past and future directions in X-ray computed tomography (CT)," *Int. J. Imaging Syst. Technol.*, vol. 12, no. 4, pp. 175–187, 2002.
[175] P. R. Smith, T. M. Peters, and R. H. T. Bates, "Image reconstruction from finite numbers of projections," *J. Phys. A, Math. Nucl. Gen.*, vol. 6, no. 3, pp. 361–382, 1973.
[176] R. M. Mersereau and A. V. Oppenheim, "Digital reconstruction of multi-dimensional signals from their projections," *Proc. IEEE*, vol. 62, pp. 1319–1338, Oct. 1974.
[177] R. A. Brooks and G. D. Chiro, "Principles of computer assisted tomography in radiographic and radio-isotopic imaging," *Phys. Med. Biol.*, vol. 21, no. 5, pp. 689–732, 1976.
[178] K. T. Smith, D. C. Solmon, and S. L. Wagner, "Practical and mathematical aspects of the problem of reconstructing objects from radiographs," *Bull. Amer. Math. Soc.*, vol. 83, no. 6, pp. 1227–1270, 1977.
[179] G. T. Herman and R. M. Lewitt, "Overview of image reconstruction from projections," in *Image Reconstruction from Projections: Implementation and Applications*, G. T. Herman, Ed. New York: Springer-Verlag, 1979, pp. 1–8.
[180] H. H. Barrett, "The Radon transform and its applications," in *Progress in Optics*, E. Wolf, Ed. New York: Elsevier, 1984, vol. 21, pp. 217–286.
[181] R. Rangayyan, A. P. Dhawan, and R. Gordon, "Algorithms for limited-view computed tomography: An annotated bibliography and a challenge," *Appl. Opt.*, vol. 24, no. 23, pp. 4000–4012, 1985.
[182] G. L. Zeng, "Image reconstruction – A tutorial," *Comput. Med. Imaging Graph.*, vol. 25, no. 2, pp. 97–103, 2001.
[183] P. P. Bruyant, "Analytic and iterative reconstruction algorithms in SPECT," *J. Nucl. Med.*, vol. 43, no. 10, pp. 1343–1358, 2002.
[184] M. Defrise, "A short reader's guide to 3D tomographic reconstruction," *Comput. Med. Imaging Graph.*, vol. 25, no. 2, pp. 113–116, 2001.
[185] C. L. Epstein, *Introduction to the Mathematics of Medical Imaging*. Upper Saddle River, NJ: Prentice-Hall Pearson, 2003.
[186] A. G. Ramm and A. I. Katsevich, *The Radon Transform and Local Tomography*. New York: CRC Press, 1996.
[187] S. Helgason, *The Radon Transform*, 2nd ed. Boston, MA: Birkhäuser, 1999.
[188] D. L. Bailey, "Transmission scanning in emission tomography," *Eur. J. Nucl. Med.*, vol. 25, no. 7, pp. 774–787, 1998.
[189] T. G. Turkington, "Attenuation correction in hybrid positron emission tomography," *Seminars Nucl. Med.*, vol. 30, no. 4, pp. 255–267, 2000.
[190] H. Zaidi and B. Hasegawa, "Determination of the attenuation map in emission tomography," *J. Nucl. Med.*, vol. 44, no. 2, pp. 291–315, 2003.
[191] S. C. Blankespoor, X. Wu, K. Kalki, J. K. Brown, H. R. Tang, C. E. Cann, and B. H. Hasegawa, "Attenuation correction of SPECT using X-ray CT on an emission-transmission CT system: Myocardial perfusion assessment," *IEEE Trans. Nucl. Sci.*, vol. 43, pp. 2263–2274, Aug. 1996.
[192] T. Beyer, D. W. Townsend, T. Brun, P. E. Kinahan, M. Charron, R. Roddy, J. Jerin, J. Young, L. Byars, and R. Nutt, "A combined PET/CT scanner for clinical oncology," *J. Nucl. Med.*, vol. 41, no. 8, pp. 1369–1379, 2000.
[193] R. J. Smith, J. S. Karp, F. Bénard, A. Alavi, E. Gualtieri, G. Muehllehner, and M. Geagan, "A comparison of segmentation and emission subtraction for singles transmission in PET," *IEEE Trans. Nucl. Sci.*, vol. 45, pp. 1212–1218, June 1998.
[194] H. Zaidi, M. Diaz-Gomez, A. Boudraa, and D. O. Slosman, "Fuzzy clustering-based segmented attenuation correction in whole-body PET imaging," *Phys. Med. Biol.*, vol. 47, no. 7, pp. 1143–1160, 2002.
[195] C. Y. Bai, P. E. Kinahan, D. Brasse, C. Comtat, and D. W. Townsend, "Postinjection single photon transmission tomography with ordered-subset algorithms for whole-body PET imaging," *IEEE Trans. Nucl. Sci.*, vol. 49, pp. 74–81, Feb. 2002.

[196] I.-T. Hsiao and G. Gindi, "Noise propagation from attenuation correction into PET reconstructions," *IEEE Trans. Nucl. Sci.*, vol. 49, pp. 90–97, Feb. 2002.
[197] D. L. Bailey, "Quantitative procedures in 3D PET," in *The Theory and Practice of 3D PET*, B. Bendriem and D. W. Townsend, Eds. Dordrecht, The Netherlands: Kluwer, 1998, pp. 55–109.
[198] L. T. Chang, "A method for attenuation correction in radionuclide computed tomography," *IEEE Trans. Nucl. Sci.*, vol. 25, pp. 638–643, Feb. 1978.
[199] P. R. Edholm, R. M. Lewitt, and B. Lindholm, "Novel properties of the Fourier decomposition of the sinogram," in *Proc. SPIE Int. Workshop Physics and Engineering of Computerized Multidimensional Imaging and Processing*, vol. 671, 1986, pp. 8–18.
[200] R. M. Lewitt, P. R. Edholm, and W. Xia, "Fourier method for correction of depth-dependent collimator blurring," in *Proc. SPIE Medical Imaging III: Image Processing*, vol. 1092, 1989, pp. 232–243.
[201] W. Xia, R. M. Lewitt, and P. R. Edholm, "Fourier correction for spatially variant collimator blurring in SPECT," *IEEE Trans. Med. Imag.*, vol. 14, pp. 100–115, Mar. 1995.
[202] P. H. Pretorius, M. A. King, S. J. Glick, T. S. Pan, and D. S. Luo, "Reducing the effect of nonstationary resolution on activity quantitation with the frequency distance relationship in SPECT," *IEEE Trans. Nucl. Sci.*, vol. 43, pp. 3335–3341, Dec. 1996.
[203] E. J. Soares, S. J. Glick, and M. A. King, "Noise characterization of combined bellini-type attenuation correction and frequency-distance principle restoration filtering," *IEEE Trans. Nucl. Sci.*, vol. 43, pp. 3278–3290, Dec. 1996.
[204] V. Kohli, M. A. King, S. J. Glick, and T. S. Pan, "Comparison of frequency-distance relationship and gaussian-diffusion-based methods of compensation for distance-dependent spatial resolution in SPECT imaging," *Phys. Med. Biol.*, vol. 43, no. 4, pp. 1025–1037, 1998.
[205] H. C. Gifford, M. A. King, R. G. Wells, W. G. Hawkins, M. V. Narayanan, and P. H. Pretorius, "LROC analysis of detector-response compensation in SPECT," *IEEE Trans. Med. Imag.*, vol. 19, pp. 463–473, May 2000.
[206] M. Defrise, "A factorization method for the 3D X-ray transform," *Inverse Problems*, vol. 11, pp. 983–994, 1995.
[207] M. Defrise, P. E. Kinahan, D. W. Townsend, C. Michel, M. Sibomana, and D. F. Newport, "Exact and approximate rebinning algorithms for 3D PET data," *IEEE Trans. Med. Imag.*, vol. 16, pp. 145–158, Apr. 1997.
[208] X. Liu, M. Defrise, C. Michel, M. Sibomana, C. Comtat, P. Kinahan, and D. Townsend, "Exact rebinning methods for three-dimensional PET," *IEEE Trans. Med. Imag.*, vol. 18, pp. 657–664, Aug. 1999.
[209] M. Defrise and X. A. Liu, "A fast rebinning algorithm for 3D positron emission tomography using John's equation," *Inverse Problems*, vol. 15, no. 4, pp. 1047–1065, 1999.
[210] C. Comtat, P. E. Kinahan, M. Defrise, C. Michel, and D. W. Townsend, "Fast reconstruction of 3D PET data with accurate statistical modeling," *IEEE Trans. Nucl. Sci.*, pt. 2, vol. 45, pp. 1083–1089, June 1998.
[211] X. Liu, C. Comtat, C. Michel, P. Kinahan, M. Defrise, and D. Townsend, "Comparison of 3-D reconstruction with 3D-OSEM and with FORE plus OSEM for PET," *IEEE Trans. Med. Imag.*, vol. 20, pp. 804–814, Aug. 2001.
[212] C. Lartizien, P. E. Kinahan, R. Swensson, C. Comtat, M. Lin, V. Villemagne, and R. Trébossen, "Evaluating image reconstruction methods for tumor detection in 3-Dimensional whole-body PET oncology imaging," *J. Nucl. Med.*, vol. 44, no. 2, pp. 276–290, 2003.
[213] J. Qi and R. H. Huesman, "Theoretical study of lesion detectability of MAP reconstruction using computer observers," *IEEE Trans. Med. Imag.*, vol. 20, pp. 815–822, Aug. 2001.
[214] H. H. Barrett, D. W. Wilson, and B. M. W. Tsui, "Noise properties of the EM algorithm. I. Theory," *Phys. Med. Biol.*, vol. 39, no. 5, pp. 833–846, 1994.
[215] C. Riddell, R. E. Carson, J. A. Carrasquillo, S. K. Libutti, D. N. Danforth, M. Whatley, and S. L. Bacharach, "Noise reduction in oncology FDG PET images by iterative reconstruction: A quantitative assessment," *J. Nucl. Med.*, vol. 42, no. 9, pp. 1316–1323, 2001.
[216] D. W. Wilson, B. M. W. Tsui, and H. H. Barrett, "Noise properties of the EM algorithm. II. Monte Carlo simulations," *Phys. Med. Biol.*, vol. 39, no. 5, pp. 847–871, 1994.
[217] J. A. Fessler, "Mean and variance of implicitly defined biased estimators (such as penalized maximum likelihood): Applications to tomography," *IEEE Trans. Image Processing*, vol. 5, pp. 493–506, Mar. 1996.
[218] W. L. Wang and G. Gindi, "Noise analysis of MAP-EM algorithms for emission tomography," *Phys. Med. Biol.*, vol. 42, no. 11, pp. 2215–2232, 1997.
[219] J. Qi and R. M. Leahy, "A theoretical study of the contrast recovery and variance of MAP reconstructions from PET data," *IEEE Trans. Med. Imag.*, vol. 18, pp. 293–305, Apr. 1999.
[220] ——, "Resolution and noise properties of MAP reconstruction for fully 3-D PET," *IEEE Trans. Med. Imag.*, vol. 19, pp. 493–506, May 2000.
[221] J. S. Liow and S. C. Strother, "The convergence of object dependent resolution in maximum likelihood based tomographic image reconstruction," *Phys. Med. Biol.*, vol. 38, no. 1, pp. 55–70, 1993.
[222] J. A. Fessler and W. L. Rogers, "Spatial resolution properties of penalized-likelihood image reconstruction: Space-invariant tomographs," *IEEE Trans. Image Processing*, vol. 5, pp. 1346–1358, Sept. 1996.
[223] L. Geworski, B. O. Knoop, M. L. de Cabrejas, W. H. Knapp, and D. L. Munz, "Recovery correction for quantitation in emission tomography: A feasibility study," *Eur. J. Nucl. Med.*, vol. 27, no. 2, pp. 161–169, 2000.
[224] B. O. Knoop, L. Geworski, M. Hofmann, D. L. Munz, and W. H. Knapp, "Use of recovery coefficients as a test of system linearity of response in positron emission tomography (PET)," *Phys. Med. Biol.*, vol. 47, no. 8, pp. 1237–1254, 2002.
[225] R. Boellaard, A. van Lingen, and A. A. Lammertsma, "Experimental and clinical evaluation of iterative reconstruction (OSEM) in dynamic PET: Quantitative characteristics and effects on kinetic modeling," *J. Nucl. Med.*, vol. 42, no. 5, pp. 808–817, 2001.
[226] J. W. Stayman and J. A. Fessler, "Regularization for uniform spatial resolution properties in penalized-likelihood image reconstruction," *IEEE Trans. Med. Imag.*, vol. 19, pp. 601–615, June 2000.

Robert M. Lewitt (Senior Member, IEEE) received the B.E. (first class honors) degree in electrical engineering and the Ph.D. degree from the University of Canterbury, Christchurch, New Zealand, in 1973 and 1977, respectively.

His research activities in the area of tomographic imaging began as a graduate student. After receiving the Ph.D. degree, he joined the Medical Image Processing Group of G.T. Herman and continued to work on various aspects of tomographic imaging, initially in Buffalo at the State University of New York (1977–1981), and then in Philadelphia at the University of Pennsylvania (1981–present), where his current position is Research Professor of Radiology. His major field of interest is research and development of computer algorithms for the reconstruction of images from projection data obtained by X-ray and gamma-ray scanners in CT, SPECT, and PET.

Samuel Matej (Senior Member, IEEE) received the M.Sc. (Honors) degree in electrical engineering from the Slovak Technical University, Bratislava, Slovak Republic, in 1983, and the Ph.D. degree in tomographic image reconstruction from the Slovak Academy of Sciences, Bratislava, Slovak Republic, in 1988.

From 1988 to 1991, he was a Research Scientist at the Institute of Measurement Sciences, Slovak Academy of Sciences. In 1991, he joined the Medical Image Processing Group, Department of Radiology, University of Pennsylvania, Philadelphia, where he is currently a Research Associate Professor of Radiology. His research interests include methods of tomographic image reconstruction from projections in PET, SPECT, CT, and MRI, with emphasis on data processing and reconstruction approaches for fully three-dimensional emission tomography.